Forcing, Cloud Feedbacks, Cloud Masking, and Internal Variability in the Cloud Radiative Effect Satellite Record

SHIV PRIYAM RAGHURAMAN,[a] DAVID PAYNTER,[b] RAYMOND MENZEL,[b,c] AND V. RAMASWAMY[a,b]

[a] *Program in Atmospheric and Oceanic Sciences, Princeton University, New Jersey*
[b] *NOAA/Geophysical Fluid Dynamics Laboratory, Princeton, New Jersey*
[c] *University Corporation for Atmospheric Research, Princeton, New Jersey*

(Manuscript received 21 July 2022, in final form 19 February 2023, accepted 22 February 2023)

ABSTRACT: Satellite observations show a near-zero trend in the top-of-atmosphere global-mean net cloud radiative effect (CRE), suggesting that clouds did not further cool nor heat the planet over the last two decades. The causes of this observed trend are unknown and can range from effective radiative forcing (ERF) to cloud feedbacks, cloud masking, and internal variability. We find that the near-zero NetCRE trend is a result of a significant negative trend in the longwave (LW) CRE and a significant positive trend in the shortwave (SW) CRE, cooling and heating the climate system, respectively. We find that it is exceptionally unlikely (<1% probability) that internal variability can explain the observed LW and SW CRE trends. Instead, the majority of the observed LWCRE trend arises from cloud masking wherein increases in greenhouse gases reduce OLR in all-sky conditions less than in clear-sky conditions. In SWCRE, rapid cloud adjustments to greenhouse gases, aerosols, and natural forcing agents (ERF) explain a majority of the observed trend. Over the northeast Pacific, we show that ERF, hitherto an ignored factor, contributes as much as cloud feedbacks to the observed SWCRE trend. Large contributions from ERF and cloud masking to the global-mean LW and SW CRE trends are supplemented by negative LW and positive SW cloud feedback trends, which are detectable at 80%–95% confidence depending on the observational uncertainty assumed. The large global-mean LW and SW cloud feedbacks cancel, leaving a small net cloud feedback that is unconstrained in sign, implying that clouds could amplify or dampen global warming.

KEYWORDS: Cloud radiative effects; Feedback; Forcing; Satellite observations; Climate models; Clouds

1. Introduction

The top-of-atmosphere cloud radiative effect (CRE) is defined as the difference between outgoing clear-sky radiative flux and all-sky radiative flux (Ramanathan et al. 1989). CRE observations by the Clouds and the Earth's Radiant Energy System (CERES) satellite (Loeb et al. 2018b) over the last two decades indicate a globally averaged longwave (LW) CRE and shortwave (SW) CRE of approximately 26 and −45 W m^{-2}, heating and cooling the climate system, respectively. Therefore, the net effect of clouds (NetCRE = LWCRE + SWCRE) is −19 W m^{-2}, cooling the planet. Even a 10% change in this quantity, approximately equal to the total present-day radiative forcing due to CO_2, would be a large change in the heat budget of the climate system (Forster et al. 2021). Despite its significance, current understanding of how CRE changes in response to external forcing is poor and how this net cooling effect of clouds changes has been a constant source of uncertainty in how much future global warming will occur (e.g., Zelinka et al. 2020). In particular, there is a lack of understanding of how observed trends in CRE, that heat or cool the climate system, have been influenced by the observed trends in greenhouse gases, aerosols, global warming (0.23 ± 0.02 K $decade^{-1}$; GISTEMP Team 2023; Lenssen et al. 2019), and internal variability. The satellite measurements of CRE provide a prime opportunity to better understand the drivers of trends in CRE and better our theoretical and modeling understanding of CRE changes.

Traditionally, a radiative change is decomposed into contributions from an external radiative forcing perturbation (solar, volcanoes, greenhouse gases, aerosols, land use, etc.) and the radiative response to this external forcing (e.g., Ramaswamy et al. 2019). Raghuraman et al. (2021a) modified this traditional forcing–feedback framework for the purposes of interpreting the observed radiation record in the context of internal variability in the climate system. Compared to the traditional framework, which is often used for large perturbations, accommodating internal variability is important for time-evolving changes in a 20-yr record. This is because observations show only one realization of the planet, but Earth could have taken many different paths due to internal variability. The observed changes in CRE, i.e., ΔCRE, are therefore a convolution of changes in effective radiative forcing (ΔERF_{CRE}), the radiative response to this forcing, i.e., warming-induced CRE change ($\Delta W_{CRE} = \lambda_{CRE}\Delta T_s$, where λ_{CRE} is the feedback that amplifies or diminishes the surface

Denotes content that is immediately available upon publication as open access.

Supplemental information related to this paper is available at the Journals Online website: https://doi.org/10.1175/JCLI-D-22-0555.s1.

Raghuraman's current affiliation: Advanced Study Program, National Center for Atmospheric Research, Boulder, Colorado.

Corresponding author: Shiv Priyam Raghuraman, shivr@alumni.princeton.edu

DOI: 10.1175/JCLI-D-22-0555.1

temperature response), and internal variability ($\varepsilon_{\mathrm{CRE}}$). An observed anomaly in CRE can thus be written as

$$\Delta\mathrm{CRE} = \Delta\mathrm{ERF}_{\mathrm{CRE}} + \Delta W_{\mathrm{CRE}} + \epsilon_{\mathrm{CRE}}. \quad (1)$$

A vast amount of previous literature has focused on how cloud changes in response to warming impact the observed radiation budget, i.e., observationally deriving cloud feedbacks ($\lambda_{\mathrm{cloud}} = \lambda_{\mathrm{CRE}} - \lambda_{\mathrm{cloud\text{-}masking}}$; appendix) (Bellomo et al. 2014; Brient and Schneider 2016; Ceppi and Nowack 2021; Cesana et al. 2019; Cesana and Del Genio 2021; Chao and Dessler 2021; Chao et al. 2022; Dessler 2010, 2013; Dessler and Loeb 2013; Lutsko et al. 2021; Myers et al. 2021; Scott et al. 2020; Yue et al. 2019; Zhou et al. 2013). However, studies have focused less on the impact of cloud feedbacks on the decadal trends in the radiation budget. Given the longer satellite record, we can now compute whether significant decadal trends in cloud feedbacks can be detected. A significant decadal trend in cloud feedback would point to a longer-term signal, as opposed to inferring cloud feedback from interannual variability.

Apart from cloud properties impacting CRE, noncloud properties such as well-mixed greenhouse gases, water vapor, temperature, and surface albedo can also impact anomalies in CRE because the existence of clouds will mask the effect of the changes in noncloud properties. This is known as cloud masking. The contributions to ΔCRE from ERF, cloud masking, and internal variability have been studied far less.

ERF constitutes instantaneous radiative forcing (IRF) and rapid cloud adjustments in response to greenhouse gases, aerosols, etc., which are separate from surface temperature-mediated feedbacks (except for the impact of land warming). The contribution of adjustments to CRE changes has been calculated in quadrupling CO_2 climate model experiments as well as cloud-resolving models (Block and Mauritsen 2013; Gregory and Webb 2008; Romps 2020; Salvi et al. 2021; Schneider et al. 2019; Wyant et al. 2012). However, there is a lack of research on ERF's contributions to the observed CRE record. Furthermore, previous regional analyses such as over the northeast Pacific have focused on cloud feedbacks and have not accounted for potential ERF contributions (Clement et al. 2009; Myers et al. 2018).

The noncloud effects, i.e., cloud masking, have been known to contribute significantly to CRE changes in climate model experiments (Soden et al. 2004, 2008). However, its contributions to observed CRE changes have been unexplored. Despite knowing that CRE in response to warming is different from the cloud feedback, CRE is still often used as proxy for cloud feedback or the potential for a contribution from ERF or cloud masking is ignored in the derivation of observational cloud feedbacks (Brient and Schneider 2016; Ceppi and Nowack 2021; Cesana et al. 2019; Cesana and Del Genio 2021; Lutsko et al. 2021; Webb and Lock 2013; Webb et al. 2015a,b, 2018; Webb and Lock 2020). This could be artificially inflating the true value of cloud feedbacks and will be explored later in this paper. When cloud masking is accounted for, it is often only used toward the goal of getting to the cloud feedback (e.g., Dessler 2010; Chao et al. 2022), instead of paying specific attention to it and being analyzed separately.

By combining and synthesizing various datasets, models, methods, and experiments, we aim to answer the following questions that will help better understand what mechanisms drive the observed CRE trends: 1) What is the range of CRE trends that can be obtained solely from internal variability? Do the observed trends lie within or outside this range? 2) What is the direct effect of greenhouse gas, aerosol, and natural forcing agent changes (ERF) on CRE trends? 3) What is surface warming's impact on the observed and modeled CRE trends? 4) How do noncloud properties such as temperature, water vapor, surface albedo affect the CRE trends? 5) What is the radiative impact of cloud changes solely due to surface warming, i.e., cloud feedback? The next section details the various observational, reanalysis, and model data used. Section 3 elucidates the climate model experiments and partial radiation perturbation experiments used in this study. Section 4 lists the results of the paper where we answer the aforementioned questions by quantifying the trends in CRE due to internal variability, ERF, cloud masking, and cloud feedbacks. Section 5 discusses the results presented. Finally, section 6 provides a summary and broader conclusions of our study.

2. Observations of ΔCRE

We use top-of-atmosphere radiative fluxes from the Clouds and the Earth's Radiant Energy System (CERES) Energy Balance and Filled (EBAF) Edition 4.1 satellite observational product (Loeb et al. 2018b) to quantify the left-hand side of Eq. (1). CERES EBAF provides clear-sky and all-sky LW, SW, and Net fluxes. The observations are provided globally at monthly-mean temporal resolution. We predominantly use the data during January 2001–December 2020 but also use the period of March 2000–June 2021. Within the clear-sky fluxes, two versions are provided: CERES "t" where observed fluxes are provided for the entire grid box and CERES "c" where observed fluxes are provided only for the clear-sky areas of the grid box (Loeb et al. 2020a). Since CERES "t" is consistent with how climate models calculate clear-sky fluxes, we use this product throughout the paper.

Although CERES is highly stable and shows close agreement in retrievals between the satellites it derives its data from, there can be uncertainties in trends arising from calibration, drift, and other observational uncertainties (Loeb et al. 2016, 2018a; Loeb and Doelling 2020; Raghuraman et al. 2021a). To that end, we attach an observational uncertainty in trends of ± 0.20 W m^{-2} decade^{-1} for clear-sky, all-sky, and CRE fluxes globally and at each grid point, following Raghuraman et al. (2021a), hereafter referred to as the R21 uncertainty. We also use an alternative observational uncertainty for trends in CRE of ± 0.085 W m^{-2} decade^{-1} given by Loeb et al. (2021b), hereafter referred to as the L21 uncertainty. The R21 uncertainty arises from Earth's energy imbalance (EEI) trend differences between different satellites CERES derives its data from as well as ocean heat uptake trends from Argo measurements. This assessed uncertainty is then assumed for CRE trends. The L21 uncertainty arises solely from CRE trend differences between CERES satellites.

TABLE 1. Summary of how each component of Eq. (1) is quantified. Temporal anomaly denoted by Δ. Acronyms: CRE = cloud radiative effect (top-of-atmosphere), CERES EBAF = Clouds and the Earth's Radiant Energy System Energy Balanced and Filled, CMIP6 = Coupled Model Intercomparison Project phase 6, GFDL AM4 = Geophysical Fluid Dynamics Laboratory Atmosphere Model 4, ERF = effective radiative forcing, SST = sea surface temperature, RFMIP = Radiative Forcing Model Intercomparison Project, W = warming-induced, PSST = prescribed SSTs and sea ice [Atmospheric Model Intercomparison Project (AMIP) conditions], H_2O = specific humidity, T_a = atmospheric temperature, T_s = surface temperature, ERA5 = European Centre for Medium-Range Weather Forecasts Reanalysis version 5, RRTMGP = Rapid Radiative Transfer Model for General Circulation Model Applications–Parallel.

Quantity	Derivation
ΔCRE	Observations of CRE from CERES EBAF Ed4.1
ε_{CRE}	2σ range of linear trends through 20-yr periods in CMIP6 Control and GFDL AM4 simulations
$\Delta\text{ERF}_{\text{CRE}}$	Transient forcing in fixed-SST simulations in RFMIP models
ΔW_{CRE}	$\Delta\text{CRE} - \Delta\text{ERF}_{\text{CRE}}$
	Observations: difference between observed ΔCRE and multimodel mean $\Delta\text{ERF}_{\text{CRE}}$. Model: 1) difference between CMIP6 ΔCRE and $\Delta\text{ERF}_{\text{CRE}}$ and 2) GFDL AM4 PSST
$\Delta W_{\text{cloud-masking}}$	$\Delta W_{\text{H}_2\text{O}} + \Delta W_{T_a} + \Delta W_{T_s} + \Delta W_{\text{surface-albedo}}$
	Partial radiation perturbation experiments with ERA5 meteorological inputs to radiative transfer model (RRTMGP)
ΔW_{cloud}	$\Delta\text{CRE} - \Delta\text{ERF}_{\text{CRE}} - \Delta W_{\text{cloud-masking}}$

In section 5, we also use the CERES FluxByCloudType (FBCT) product (Sun et al. 2022) to better understand the vertical structure of the observed CRE trends. We calculate CRE in CERES-FBCT by differencing the clear-sky and the all-sky fluxes for each grid box, following Eq. (5) of Scott et al. (2020). Finally, to calculate observed surface temperature-induced feedbacks, we use NASA GISTEMP surface temperature anomalies (Lenssen et al. 2019). Although observations provide unprecedented information about the changing nature of CRE, deciphering the causes of the trends in CRE from observations alone is difficult. To understand the causes, we conduct a range of model experiments that are described below.

3. Methods

Below we describe each component on the right-hand side of Eq. (1), and the components are summarized in Table 1.

a. *Internal variability (ε_{CRE}): CMIP6 Control and AM4 Control*

We use 41 models' outputs of TOA radiation in clear-sky and all-sky, LW and SW radiation from experiments in the Coupled Model Intercomparison Project phase 6 (CMIP6) archive (Eyring et al. 2016). We use the preindustrial control experiment for each model, wherein forcing agents are fixed at 1850 values and the coupled models have freely evolving lower boundary conditions. We use this experiment, labeled as "CMIP6 Control" in the rest of the paper, to diagnose the range of trends in CRE that can occur in a 20-yr period, arising solely from internal variability. We use consecutive, nonoverlapping 20-yr periods in each model (in total 1144 periods/realizations) and the $\pm 2\sigma$ range of trends in these 20-yr periods is ε_{CRE}.

We conduct another control experiment wherein we quantify the trends in 20-yr periods arising solely from atmospheric stochasticity, as opposed to the CMIP6 Control simulations which contain both atmospheric and oceanic variability. Using GFDL's atmosphere-only model AM4 (Zhao et al. 2018), we prescribe SSTs taken from a climatological GFDL CM4 preindustrial control experiment and repeat these same SSTs year-on-year (fixed SSTs) to produce a 200-yr time series (AM4 Control). To create a longer time series, this is then bootstrapped to further form a 2000-yr time series. We calculate the trend in each of the one-hundred 20-yr consecutive, nonoverlapping periods. The $\pm 2\sigma$ range of these 100 trends provides us another estimate of ε_{CRE}. Finally, we conduct an initial condition large ensemble (20 realizations) experiment which allows radiative forcing agents (well-mixed greenhouse gases, ozone, anthropogenic sulfate, and black carbon) to vary during 2001–20 in addition to the prescribed SSTs and sea ice (AM4 PSST + ERF) (used in Raghuraman et al. 2021a). This experiment provides the total CRE, i.e., the sum of the ERF and radiative response $\Delta\text{ERF}_{\text{CRE}} + \Delta W_{\text{CRE}}$ as well as another estimate of the internal variability ε_{CRE}.

b. *Effective radiative forcing (ΔERF_{CRE}): RFMIP*

To better understand how much of the modeled CRE changes arise from forcing versus feedback, we analyze 7 of the 41 models above that provided estimates of the effective radiative forcing during 2001–20. This has been made possible by the transient forcing experiments in the Radiative Forcing Modeling Intercomparison Project (RFMIP) which simulates forcing agent changes in the model with SSTs fixed (Pincus et al. 2016). Each model produced three realizations (unless otherwise stated) and provided a further breakdown of all forcing agents (piClim-histall) into its contributions from greenhouse gases (piClim-histghg), aerosols (piClim-histaer), and natural forcing (solar and volcanic) (piClim-histnat). We note that recent updates to the Community Emissions Data Systems (CEDS) show larger decays in global aerosol emission than previous release versions (Hoesly et al. 2018; O'Rourke et al. 2021), thereby underestimating the aerosol emission decreases used in

this study. Finally, the difference between AM4 PSST + ERF and AM4 PSST (described below; both used in Raghuraman et al. 2021a) provides another estimate of ΔERF_{CRE}, which will be used alongside RFMIP's estimates.

c. *Warming-induced CRE (ΔW_{CRE}): Observational derivation, coupled models, and AMIP*

First, we obtain an observationally derived ΔW_{CRE}, i.e., the CRE radiative response, by subtracting the RFMIP multimodel mean ΔERF_{CRE} from the observed ΔCRE. Since warming-induced CRE could include internal variability, we attach the measure of internal variability uncertainty (ε_{CRE} from CMIP6 Control) to the observed ΔW_{CRE}. Second, we quantify ΔW_{CRE} in seven coupled models by subtracting ΔERF_{CRE} from their Historical (2001–14) + SSP2-4.5 (2015–20; Gidden et al. 2019) ΔCRE simulations. Third, we quantify ΔW_{CRE} over this period in GFDL AM4 with AMIP conditions. We simulate an initial condition large ensemble (20 realizations) experiment of 2001–20 radiative fluxes with GFDL AM4 with prescribed SSTs and sea ice (AMIP) and radiative forcing fixed at 2014 levels (AM4 PSST). The mean of this ensemble's trends provides the best estimate of the radiative response (ΔW_{CRE}) and the 2σ range of trends provides another estimate of ε_{CRE}.

We note here the distinction between what we term ERF versus radiative response/feedback. This distinction is important to consider since parts of ERF could be considered as "feedbacks" especially when viewed from the observational perspective. For example, despite having fixed SSTs in the RFMIP simulations, models will have a land warming impact that may impact CRE (Andrews et al. 2021). This land warming is considered to be a part of the ERF component rather than the response/feedback component. Therefore, in this study, we assume that ERF arises from forcing agent changes without SST changes while radiative response/feedback arises from SST changes without forcing agent changes.

d. *Decomposing ΔCRE into cloud and cloud-masking contributions: PRP experiments*

To decompose fluxes in an alternate manner that focuses on particular processes, we employ the partial radiation perturbation (PRP) method. This method has been used extensively over the last few decades for climate feedback decompositions (e.g., Colman and McAvaney 1997; Soden et al. 2008) and more recently has also been used for decompositions of observed time series fluxes (e.g., Clark et al. 2021; Raghuraman et al. 2019; Thorsen et al. 2018). PRP is used here to isolate the radiative impact of a particular quantity's temporal change, i.e., we quantify the contributions to ΔCRE from changes in water vapor, surface temperature, atmospheric temperature (including stratospheric temperature), surface albedo, well-mixed greenhouse gases, ozone, and clouds. It allows us to decompose ΔCRE into the sum of contributions from cloud changes and noncloud changes, also known as cloud-masking changes. We refer the reader to the appendix for further details.

To conduct the PRP experiments, we use reanalysis meteorological monthly-mean data as input for an offline radiative transfer model called the Rapid Radiative Transfer Model for General Circulation Model Applications–Parallel (RRTMGP) (Pincus et al. 2019). Computing all-sky fluxes required a careful treatment of cloud overlap, coverage, etc., so we stochastically generate 10 subcolumns for each grid box following Pincus et al. (2006) and Tompkins (2002). We used the European Centre for Medium-Range Weather Forecasts Reanalysis version 5 (ERA5; Hersbach et al. 2020) product's meteorological quantities for the PRP experiments (appendix). We found that ERA5's outputs of TOA radiation variability and trends had higher fidelity in matching observations compared to MERRA-2 (Fig. 1 in the online supplemental material; Gelaro et al. 2017). Finally, we used NOAA's annual greenhouse gas index (AGGI) data, which compiles observations of CO_2, CH_4, N_2O, CFCs, and HFCs concentrations up to present day (Hofmann et al. 2006).

e. *Cloud feedback: Observational derivation*

ΔCRE is the sum of the cloud and cloud-masking components [Eq. (A3c)]. We use the PRP decomposition to quantify the warming-induced cloud masking present in ΔCRE and obtain the satellite-derived cloud feedback by subtracting this warming-induced cloud masking as well as RFMIP's ΔERF_{CRE} from the observed CRE [Eq. (A4b)]. This method is commonly used in previous studies that obtained observational cloud feedbacks (e.g., Dessler 2013). Since cloud feedbacks could include internal variability, we attach the measure of internal variability uncertainty (ϵ_{CRE} from CMIP6 Control) to the observed LW, SW, and Net cloud feedbacks. Observational and internal variability uncertainties are combined in quadrature.

4. Results

a. *Internal variability (ϵ_{CRE})*

As shown in Figs. 1a and 1c (and the accompanying time series in supplemental Fig. 2), CERES LWCRE and SWCRE trends are statistically significant after accounting for observational uncertainty. However, it is unclear how these observed trends should be interpreted, i.e., what is the context of these trends in the presence of internal variability on the planet? In Figs. 1a, 1c, and 1e, we plot the probability distribution of all the 20-yr CRE trends (in total 1144 trends) from the CMIP6 Control experiment. We find that for LW, SW, and Net CRE, each control distribution's mean is centered at 0 and follows a Gaussian distribution. In LWCRE, the spread of possible trends in a 20-yr period due to internal variability is narrow, i.e., $\epsilon = \pm 0.08$ W m^{-2} decade^{-1}. In SWCRE and NetCRE, they have wider ranges: $\epsilon = \pm 0.18$ and ± 0.16 W m^{-2} decade^{-1}, respectively.

CERES trends in LWCRE and SWCRE are -0.35 and 0.33 W m^{-2} decade^{-1}, respectively, which are 2–4 times larger than ϵ. Even when a conservative estimate of observational uncertainty is used on the CERES trends (± 0.20 W m^{-2} decade^{-1}, R21 uncertainty) as a normal distribution, the probability that internal variability alone caused the observed LW and SW CRE trends is exceptionally unlikely (<1%; Mastrandrea et al. 2010). For example, in the case CERES SWCRE, the probability that a trend from CMIP6 Control has a large trend (>0.16 W m^{-2} decade^{-1};

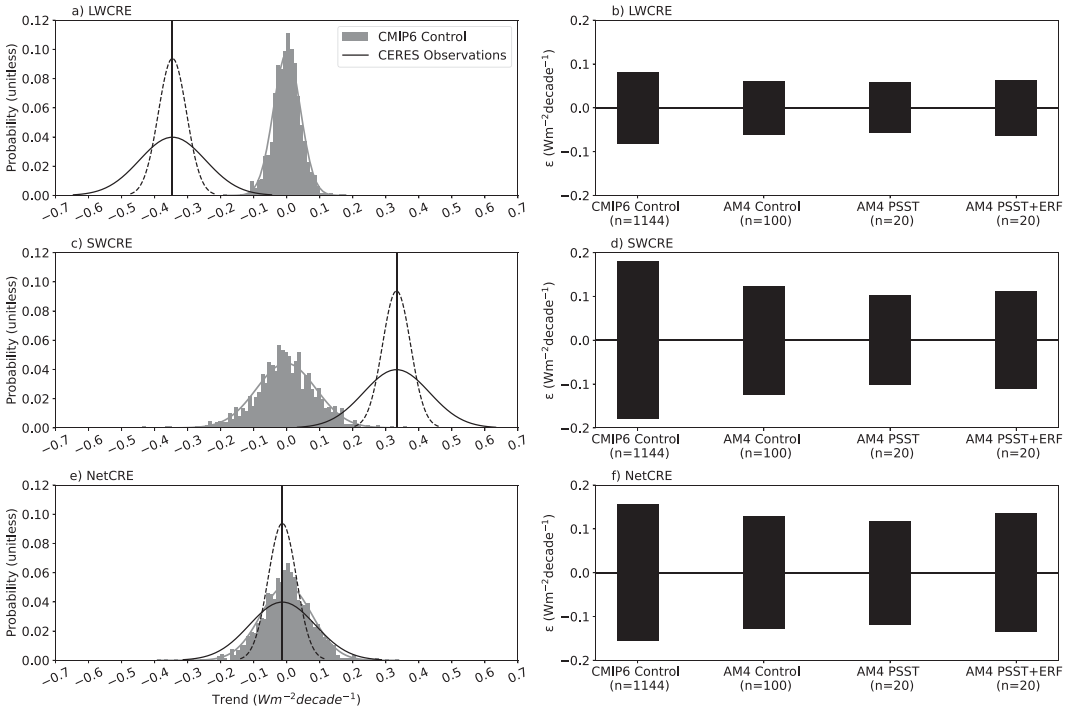

FIG. 1. 2001–20 CERES trends and internal variability trends. (a) Probability distributions of LWCRE trends in CERES observations (assumed to be Gaussian) and CMIP6 Control LWCRE trends in 20-yr periods. (b) Range of trends due to internal variability in various model ensembles; *n* represents number of realizations (trends in 20-yr periods). (c) As in (a), but for SWCRE. (d) As in (b), but for SWCRE. (e) As in (a), but for NetCRE. (f) As in (b), but for NetCRE. Solid lines and dashed lines represent R21 and L21 observational uncertainties, respectively.

point of intersection of the two curves) is ~3.6%, and the probability that CERES had a small trend due to drift or other observational uncertainties (<0.16 W m^{-2} $decade^{-1}$) is ~4.2%. The probability of whether these two events occur in the same 20-yr period is what is of interest to this study. Since these are independent events, the probabilities can be multiplied which yields ~0.15%. If a uniform distribution or a skewed normal distribution is instead used on the observational trends, this probability would be slightly larger but would still be exceptionally unlikely.

We found that as more years are added to the time period, the range of trends (ϵ_{CRE}) reduces exponentially (supplemental Fig. 3). By 2020, the observed LW and SW CRE trends are detectable over observational uncertainty and internal variability. By 2030, LWCRE ϵ will decrease further by 60%, SWCRE ϵ will decrease further by 35%, and NetCRE ϵ will decrease further by 30% (in GFDL CM4 Control). These results are consistent with other studies who also showed large decreases in uncertainty due to internal variability with time (Loeb et al. 2022; Raghuraman et al. 2021a; Zhou et al. 2015). This can also be seen in observed CRE trends wherein the trends vary substantially when only less than a decade of data are used but converges on a long-term value when closer to two decades of data are used at which point the observed trends are insensitive to start and end dates (supplemental Fig. 4). Overall, these results show the value of a continuous climate data record of Earth radiation budget changes (Shankar et al. 2020).

We find that the ϵ_{CRE} obtained from the coupled model GFDL CM4 is similar to the ϵ values in the hierarchy of the atmosphere-only model GFDL AM4 experiments in LWCRE, SWCRE, and NetCRE (Figs. 1b,d,f). This implies that ϵ is unaffected by forcing and feedbacks in our experiments because it was unchanged under a range of boundary conditions and forcings: freely evolving SSTs (CM4 Control), fixed SSTs (AM4 Control), prescribed SSTs (AM4 PSST), and prescribed SSTs and ERF (AM4 PSST + ERF). Overall, CERES LW and SW CRE trends lie outside the realm of internal variability whether generated by coupled models or an atmosphere-only model. Interestingly, the NetCRE CERES trend seems to be a part of the internal variability ensemble. However, we now know that this is due to the strong LW and SW CRE trends that are detectable above observational uncertainty and internal variability which cancel to yield a weak NetCRE trend. This cancellation suggests a role of external forcing and feedbacks in the observed LW and SW CRE trends, which is explored below.

b. *Effective radiative forcing (ΔERF_{CRE})*

We next explore the role of radiative forcing in the observed CRE trends. We analyze ΔERF_{CRE} trends over 2001–20 period from the seven models participating in the RFMIP historical forcing experiments, which arise from instantaneous radiative forcing as well as adjustments which are not sea surface temperature mediated. We find significant trends in LWCRE, SWCRE, and NetCRE due to all

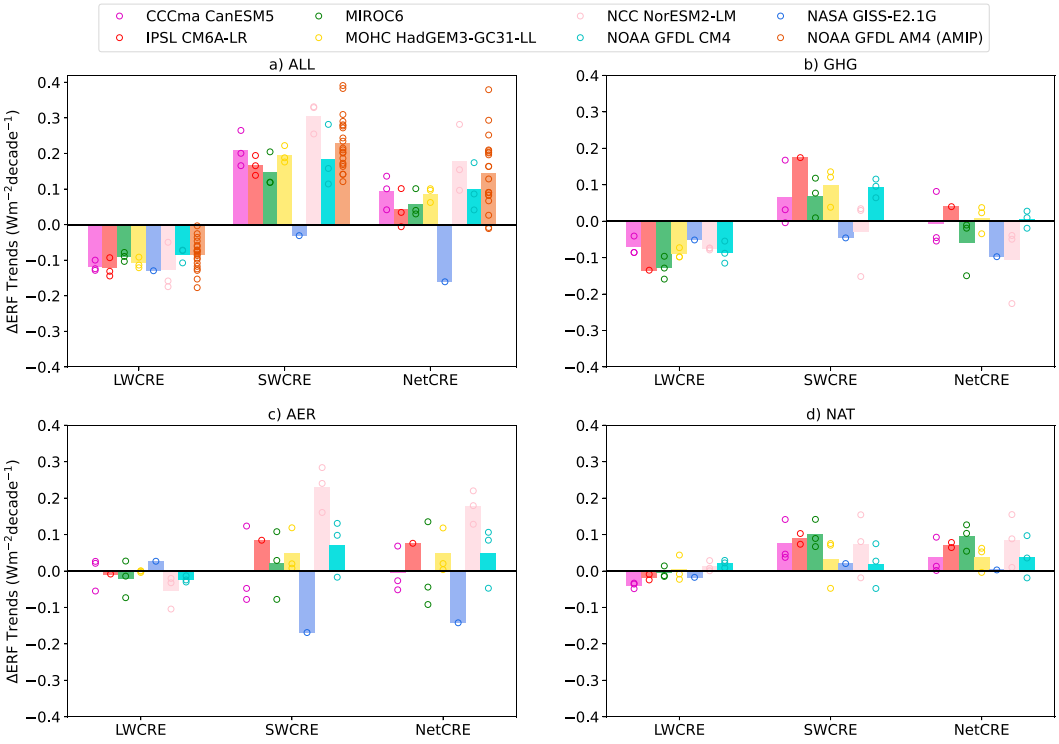

FIG. 2. 2001–20 global-mean trends in effective radiative forcing in LWCRE, SWCRE, and NetCRE. Each realization is represented by a hollow circle and the mean is represented by the bar. (a) All forcing agents varying. (b) Greenhouse gases only varying. (c) Aerosols only varying. (d) Natural forcing agents only varying.

forcing agents. The multimodel mean ΔERF_{LWCRE} trend is -0.11 ± 0.01 W m^{-2} decade^{-1}, ΔERF_{SWCRE} trend is 0.19 ± 0.04 W m^{-2} decade^{-1}, and the ΔERF_{NetCRE} trend is 0.08 ± 0.04 W m^{-2} decade^{-1} (95% CI about the mean) (Fig. 2a). This result is robust across models (barring NASA GISS-E2.1-G in SWCRE and hence NetCRE). Thus, the negative trend in ΔERF_{LWCRE} can help explain the observed negative trend in LWCRE and the positive trend in ΔERF_{SWCRE} alone could potentially explain the majority of the observed positive trend (~57%).

Given these significant ΔERF_{CRE} trends arising from all forcing agents acting together, it is important to understand the contributions from each agent. The negative trend in ΔERF_{LWCRE} from all forcing agents predominantly arises from greenhouse gas increases over the period (Fig. 2b). In section 4d we will further explore the source of this trend using an offline radiative transfer model. The positive trend in ΔERF_{SWCRE} from all forcing agents can be seen to arise from changes in greenhouse gases, aerosols, and natural forcing agents (Figs. 2b–d). It has been shown in large-eddy simulations that the increase in greenhouse gases decreases cloud-top radiative cooling which decreases cloud cover although this has not been confirmed in climate models (e.g., Schneider et al. 2019). This cloud cover decrease in turn decreases reflection of sunlight particularly over the west coasts of continents where low-lying clouds are pervasive which is seen in AM4 (supplemental Fig. 5, Fig. 2b).

The decrease in aerosols in the midlatitudes, particularly over the United States and Europe (Loeb et al. 2021a), has been shown recently to cause a decrease in liquid water path in AM4 via the second aerosol indirect effect (Raghuraman et al. 2021a), however this is model dependent (Fig. 2c). This decreases reflection of sunlight by clouds, i.e., a positive trend in SWCRE. In addition to aerosol-heavy regions in the midlatitudes, a positive ΔERF_{SWCRE} trend due to aerosols were found to contribute over oceanic regions too, which previous studies have pointed toward too (e.g., Wilcox et al. 2006). We note that Community Emissions Data Systems (CEDS) indicates larger aerosol decays so our ΔERF_{SWCRE} trends due to aerosols alone may be even more positive. By the end of the century, however, the greenhouse gas adjustments dominate over the aerosol and natural components (supplemental Fig. 5). We also found that models largely imitate the global-mean results (Fig. 2) in the tropical mean too (supplemental Fig. 6).

We further probe the observed positive SWCRE trend and its causal factors. In Fig. 3a, we show that the global-mean CERES-observed positive SWCRE trend manifests spatially too as a positive trend across large swaths of the ocean as well as some land portions. We focus on the northeast Pacific to show how important the ERF contribution to SWCRE is. ERF was not considered in previous analyses and the change in northeast Pacific reflection was assumed to only be SST-driven (Andersen et al. 2022; Loeb et al. 2018a, 2020b; Myers et al. 2018). Figure 3b shows that the ΔERF_{SWCRE} trend magnitude is as large as the SST-mediated SWCRE response (AM4 PSST). We find that this is partly because low cloud

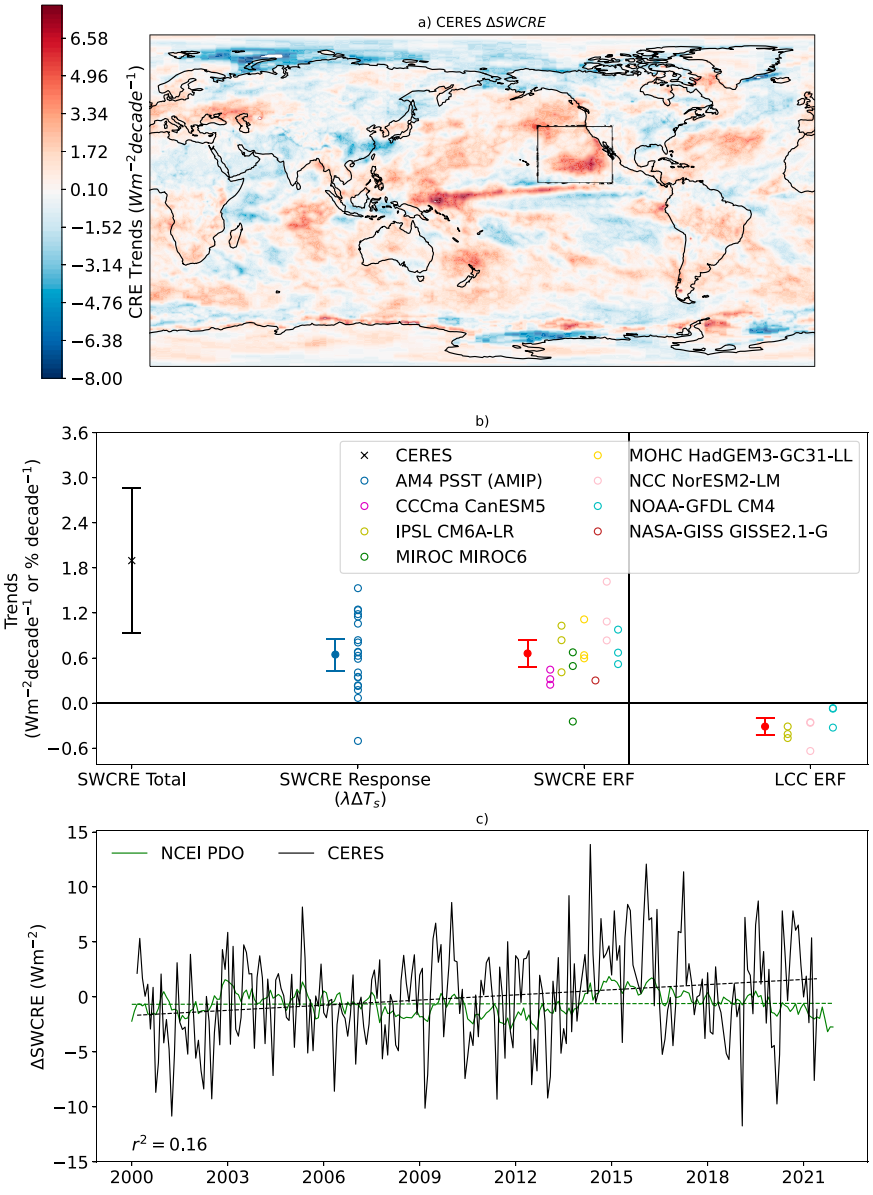

FIG. 3. (a) Spatial pattern of CERES-observed SWCRE trends. (b) Trends in SWCRE in CERES, AM4 PSST, and RFMIP models over the northeast Pacific region [outlined by the box in (a) and follows the Loeb et al. (2020b) definition]. Trends in low cloud cover over the northeast Pacific region arising solely from ERF are plotted for a subset of RFMIP models. Hollow circles represent each 20-yr trend and the ensemble means are plotted in filled circles. Red filled circle represents multimodel mean. Error bars represent the 95% CI around the mean. In CERES's case this represents observational uncertainty and internal variability uncertainty (standard error associated with linear fit). In the models' case the 95% CI is given by $1.96 \times \sigma/\sqrt{n}$, where σ is the standard deviation of the ensemble's trends and n is the number of realizations. (c) Time series of the CERES-observed SWCRE monthly anomalies over the northeast Pacific region and the Pacific decadal oscillation index. The r^2 value between the curves is noted. Dashed lines indicate trends.

cover in response to forcing alone showed a decrease of 0.3% $decade^{-1}$ for the subset of models that outputted this quantity. Importantly, we find that the positive ΔERF_{SWCRE} trend is robust across models. Although the response and ERF when summed together would fall into CERES' uncertainty range, they underestimate the central CERES trend value.

Previous work has also assumed much of the observed SWCRE change in the northeast Pacific can be attributed to

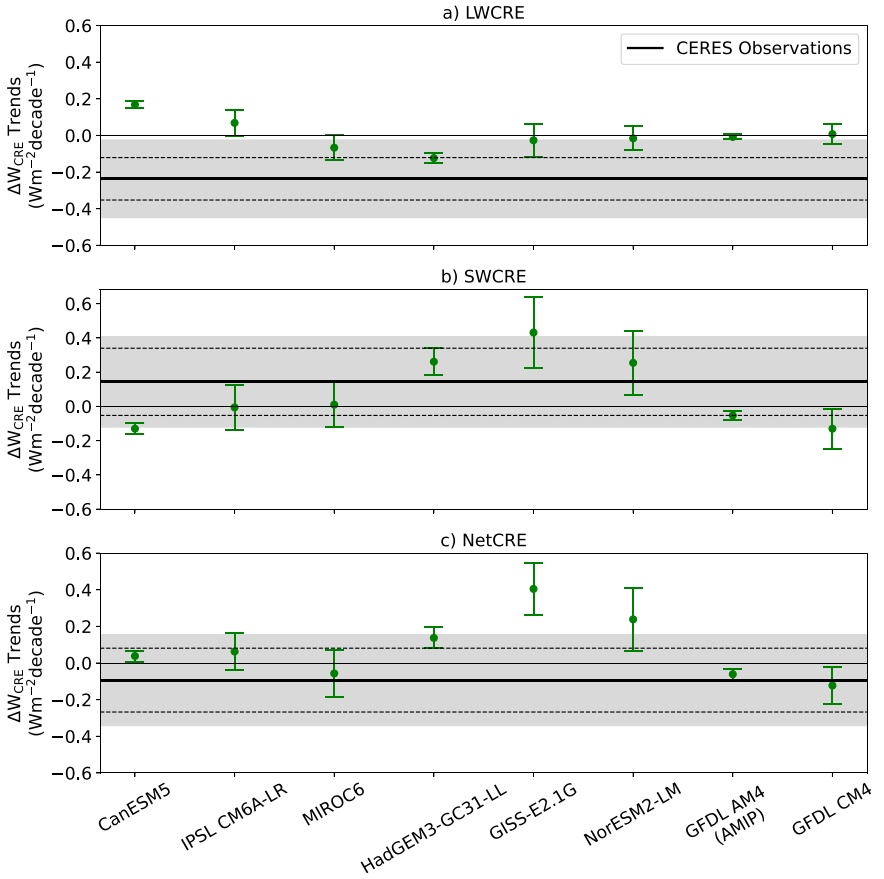

FIG. 4. Global-mean observationally derived and modeled warming-induced CRE trends during 2001–20. (a) LWCRE. (b) SWCRE. (c) NetCRE. Shading indicates the 95% CI comprising internal variability uncertainty ($\varepsilon_{\mathrm{CRE}}$ from CMIP6 Control) and R21 observational uncertainty. Dashed lines represent uncertainty due to internal variability uncertainty and L21 observational uncertainty. Green error bar represents model's 95% CI ($1.96 \times \sigma/\sqrt{n} \sim \varepsilon_{\mathrm{CRE}}/\sqrt{n}$, where n represents the number of realizations). GISS-E2.1-G in p1f2 configuration. GFDL AM4 given by AM4 PSST experiment.

the Pacific decadal oscillation (PDO) (Loeb et al. 2018a, 2020b, 2021b). Figure 3b shows that a large range of SST-mediated SWCRE trends are possible, despite giving the model the same AMIP SST pattern in each realization (which contains the PDO). Thus, due to atmospheric noise, the same SST pattern and PDO can yield a negative, near-zero, or positive trend in SWCRE (Fig. 3b, SWCRE response). Furthermore, we show that, the PDO index and CERES SWCRE over the northeast Pacific are poorly correlated and the trend in the PDO index is near-zero while CERES SWCRE over the northeast Pacific is strongly positive (Fig. 3c). Loeb et al. (2021b) argued that the change in sign of the PDO in 2014 can help explain TOA radiation trends, however, Fig. 3c shows that PDO started shifting back to a negative phase in 2018, yet SWCRE continues to have a positive trend in the northeast Pacific. In summary, over the northeast Pacific we show that 1) ERF has a large responsibility for the reflection decrease, 2) an SST pattern supported this reflection decrease, and 3) the PDO is not the SST pattern that caused this long-term reflection decrease.

c. *Warming-induced CRE (ΔW_{CRE})*

Given the important roles ERF and ϵ play in the CRE trends' magnitudes and uncertainty, the observed CRE trends thus cannot be attributed solely to the warming-induced CRE trends [Eq. (1)]. We obtain an observationally derived ΔW_{CRE} trend by subtracting the RFMIP multimodel mean $\Delta \mathrm{ERF}_{\mathrm{CRE}}$ trend from the observed ΔCRE trend and attach to it observational uncertainty and internal variability uncertainty (ϵ_{CRE}) (Fig. 4). The results remain the same when calculating the observationally derived ΔW_{CRE} trend eight different times with each RFMIP model instead of using the multimodel mean $\Delta \mathrm{ERF}_{\mathrm{CRE}}$ trend (supplemental Fig. 7). We find that the observationally derived $\Delta W_{\mathrm{LWCRE}}$ trend is negative, implying that surface warming decreases LWCRE, cooling the climate system. Its mechanisms will be explained in the next subsection. On the other hand, the observationally derived $\Delta W_{\mathrm{SWCRE}}$ trend is positive but is not statistically significant, i.e., the SWCRE warming response could either heat or cool

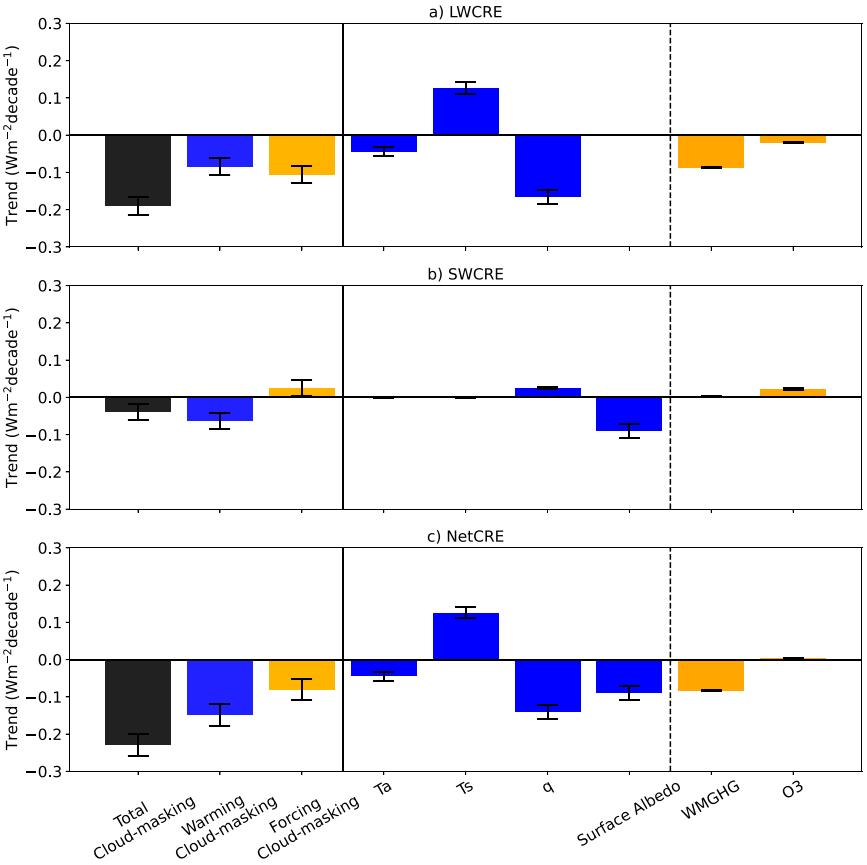

FIG. 5. Trends in ERA5-PRP cloud-masking components during January 2001–December 2020: (a) LWCRE, (b) SWCRE, and (c) NetCRE. Blue (orange) bar in the left third of each panel arises from sum of individual quantities' blue (orange) bars. Black bar is the sum of the warming-induced cloud masking and forcing-induced cloud masking. Error bars given by the 95% confidence intervals derived from the standard error of the linear fit.

the climate system. As a result, the NetCRE warming response could also either heat or cool the climate system.

CMIP6 models' ΔW_{CRE} estimates are also provided using the CMIP6 Historical and RFMIP ERF experiments. The robust agreement in $\Delta \mathrm{ERF}_{\mathrm{CRE}}$ between these models in Fig. 2 stands in sharp contrast to the wide range of CRE responses to surface warming in Fig. 4. The $\pm 2\sigma$ range (intermodel spread) of $\Delta \mathrm{ERF}_{\mathrm{CRE}}$ trends across models for LWCRE, SWCRE, and NetCRE is ± 0.06, ± 0.16, and ± 0.17 W m^{-2} decade^{-1}, respectively. The $\pm 2\sigma$ range (intermodel spread) of ΔW_{CRE} estimates across models for LWCRE, SWCRE, and NetCRE is ± 0.17, ± 0.39, and ± 0.33 W m^{-2} decade^{-1}, respectively; approximately 2–3 times larger than the $\Delta \mathrm{ERF}_{\mathrm{CRE}}$ model spread.

Even after accounting for observational and internal variability uncertainties on the observed trends, three of the seven models disagree with the observationally derived $\Delta W_{\mathrm{LWCRE}}$ [CanESM5, IPSL CM6A-LR, and GFDL AM4 (AMIP)]. These models simulate either a positive or neutral LWCRE response to warming instead of the observed negative response. In $\Delta W_{\mathrm{SWCRE}}$ and $\Delta W_{\mathrm{NetCRE}}$, models largely agree with observations barring NASA GISS-E2.1-G. This model increases NetCRE dramatically in response to warming (mostly due to the SWCRE response), while observations show a much more muted NetCRE response to warming. Using the L21 uncertainty as a stricter test for climate models, only one model, MIROC6, falls into the observed trends range for all three CRE budget terms (LW, SW, and Net). Importantly, we show that the AMIP and coupled simulations of GFDL agree strongly with each other. This suggests that any underestimation of the CERES trends arises from problems in the physics of the atmospheric component of the model.

d. *Cloud-masking contributions*

So far, we have dealt with the total CRE change and its contributions from ϵ_{CRE}, $\Delta \mathrm{ERF}_{\mathrm{CRE}}$, and ΔW_{CRE}. However, these changes could be due to the cloud properties changing or cloud-masking properties changing. In this section we attempt to understand the possible role of each, with the eventual aim to understand the possible range of cloud feedbacks attributable to the observed CRE record, using the PRP method (section 3d). The total CRE change is the sum of the cloud-induced changes and the non-cloud-induced changes, i.e., cloud-masking changes (appendix). In this subsection we analyze the trends in CRE due to the cloud masking of water

TABLE 2. Global-mean cloud masking estimates across a range of models, data, and experiments. Ensemble means are presented for studies that included multiple models or multiple experiments. Each study computes the cloud masking by PRP or radiative kernels technique. Soden et al. (2004) values are taken from their Fig. 2 (difference between PRP and CRF). Soden et al. (2008) values are taken from their Fig. 10; LWCRE and SWCRE breakdown was not provided so we assume water vapor + temperature = LW and SW = surface albedo. Yoshimori et al. 2020 values are taken from their Tables 1 and 2; we again use water vapor + temperature = LW. Sign convention: positive implies heating and negative means cooling. Uncertainty given by the 95% CI. Barring the ERA5 row from this study, all estimates are derived from multiplying the literature values by the 2001–20 GISTEMP-observed surface warming trend of 0.23 K decade^{-1}. Units in the three right columns are W m^{-2} decade^{-1}. GFDL = NOAA Geophysical Fluid Dynamics Laboratory. IPCC AR4 = Intergovernmental Panel on Climate Change Assessment Report 4. MIROC5.2-A = Model for Interdisciplinary Research on Climate 5.2-Atmosphere. HadGEM2-A = Hadley Centre Global Environment Model version 2–Atmosphere. ERA5 = European Centre for Medium Range Forecasts Reanalysis 5. SST = sea surface temperature. AMIP = Atmospheric Modeling Intercomparison Project. TCR = Transient Climate Response.

Study	Model/data	Experiments	LWCRE	SWCRE	NetCRE
Soden et al. (2004)	GFDL AM2	SST ± 2 K	−0.11	0.03	−0.07
Soden et al. (2008)	IPCC AR4	2000–2100 A1B Scenario	−0.09	−0.06	−0.15
Yoshimori et al. (2020)	MIROC5.2-A, HadGEM2-A	AMIP, AMIP + 4 K	−0.12	—	—
This study (Raghuraman et al. 2023)	GFDL AM3, GFDL AM4	TCR	−0.10	−0.06	−0.15
This study (Raghuraman et al. 2023)	ERA5-PRP	2001–20	−0.08 ± 0.02	−0.06 ± 0.02	−0.15 ± 0.03

vapor, surface temperature, atmospheric temperature, surface albedo, well-mixed greenhouse gases, and ozone individually without discriminating whether it belongs to the forcing component or the feedback component. In the next subsection, to calculate cloud feedbacks, we assign particular quantities to forcing versus feedback.

Before we breakdown the drivers of the cloud-masking trends (Fig. 5 and supplemental Fig. 8), we first establish confidence in our ERA5-PRP cloud-masking calculations. First, ERA5-PRP clear-sky fluxes compare well with CERES not only in trends but also in variability too (supplemental Fig. 1); signaling accurate representations of water vapor, temperature, and surface albedo in ERA5. Second, ERA5's climatological clouds are highly similar to observations in their spatial pattern (Wu et al. 2022; Yao et al. 2020). Together, the radiative impact of noncloud properties in the presence of clouds is well captured by ERA5-PRP. We will further show below that the ERA5-PRP cloud-masking estimates are in agreement with previous estimates.

LWCRE shows strong cloud-masking trends and the total cloud-masking trend could account for ~57% of observed trend (Fig. 5a). This negative LWCRE trend largely arises from greenhouse gases: water vapor, well-mixed greenhouse gases, and ozone. This occurs because the increase in greenhouse gases significantly decreases clear-sky OLR but decreases all-sky OLR by not as much (−0.88 versus −0.61 W m^{-2} decade^{-1}). This is because when clouds are introduced into the column, greenhouse gases and clouds compete for the same photons, lessening the impact of the greenhouse gas increase on the top-of-atmosphere flux (Soden et al. 2008; Yoshimori et al. 2020). The instantaneous radiative forcing cloud masking from well-mixed greenhouse gases and ozone is −0.11 W m^{-2} decade^{-1}. This offline radiative transfer calculation is identical to the ERF calculated from climate models (Fig. 2b), suggesting that cloud-masking IRF is the dominant component of $\Delta \mathrm{ERF}_{\mathrm{LWCRE}}$ or suggesting there is a cancellation of adjustments.

SWCRE cloud masking is negative mostly due to surface albedo changes (Fig. 5b). Given the decrease in sea ice and land ice over this period, reflected shortwave radiation (RSW) decreased significantly in clear-skies (Raghuraman et al. 2021a). From a top-of-atmosphere perspective, when clouds are introduced into the column, the albedo decreases occurring at the surface are unable to be effectively communicated to space in all-sky RSW (Soden et al. 2008). Thus, clouds are masking underlying surface albedo trends and results in a negative SWCRE cloud-masking trend. It follows that these negative cloud-masking trends in LWCRE and SWCRE result in a large, negative, cloud-masking trend in NetCRE (Fig. 5c). Overall, these ERA5-PRP calculations of cloud masking agree well with previous studies' estimates of cloud masking (Table 2). In particular, the agreement across generations of GFDL models, different climate models, different experiments, and different techniques suggests that our understanding of the cloud masking component stands on a strong foundation.

e. *Cloud feedback: Observational derivation*

Although the cloud component of CRE is available from the PRP experiments (supplemental Fig. 8), we do not use it as an estimate of cloud feedback since 1) the reanalysis clouds likely contain the forcing component from greenhouse gases, aerosols, etc., so $\Delta \mathrm{CRE}_{\mathrm{cloud}}$ is a mixture of forcing and feedback and would not give us the desired separated cloud feedback and 2) ERA5-PRP produces incorrect all-sky fluxes compared to CERES (supplemental Fig. 1). We thus use our PRP estimate of cloud masking to convert our estimate of ΔW_{CRE} to cloud feedback [Eqs. (A3c) and (A4b)]. As is common in previous studies (e.g., Soden et al. 2008), we assume atmospheric temperature, surface temperature, water vapor, and surface albedo contributions to CRE predominantly belong to the warming-induced component of CRE rather than the forcing and adjustments component. This allows us to compute the cloud feedback component of the CRE trend from observations [$\Delta W_{\mathrm{cloud}} = \Delta \mathrm{CRE} - \Delta \mathrm{ERF}_{\mathrm{CRE}} - \Delta W_{\mathrm{cloud\text{-}masking}}$; Table 1; Eq. (A4b)].

The contributions to CRE trends from ERF, cloud masking, and cloud feedback and the associated observational

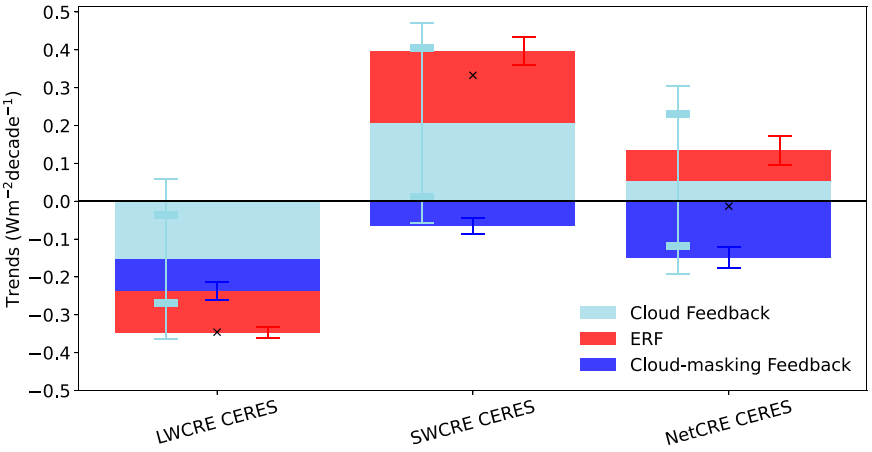

FIG. 6. Summary of contributions to ΔCRE trends from forcing (ΔERF_{CRE}; RFMIP multimodel mean), cloud masking ($\Delta W_{cloud\text{-}masking}$; ERA5-PRP), and cloud feedbacks ($\Delta CRE - \Delta ERF_{CRE} - \Delta W_{cloud\text{-}masking}$) for the global-mean January 2001–December 2020 period. Sum of the individual bars represent the observed CRE trend and is labeled with a cross sign. Error bars represent the 95% CI. Cloud feedback error bars arise from observational uncertainty and ε_{CRE}. Thin and thick bars given by R21 and L21 uncertainties, respectively, for the observational uncertainty component.

uncertainty and internal variability uncertainty are summarized in Fig. 6 for the global-mean case. LWCRE ERF and cloud masking were both negative, yielding a negative cloud feedback that supplements it. This LW cloud feedback trend is significant at 80% confidence with R21 observational uncertainty (-0.15 ± 0.14 W m^{-2} decade^{-1}) and 95% confidence with L21 observational uncertainty (-0.15 ± 0.12 W m^{-2} decade^{-1}). SWCRE ERF was strongly positive while SWCRE cloud masking was weakly negative, yielding a positive SW cloud feedback. This SW cloud feedback trend is significant at 85% confidence with R21 observational uncertainty (0.21 ± 0.19 W m^{-2} decade^{-1}) and 95% confidence with L21 observational uncertainty (0.21 ± 0.20 W m^{-2} decade^{-1}). As a result of these significant LW and SW cloud feedback trends of opposing signs, the net cloud feedback trend is only slightly positive and not significant with either R21 or L21 uncertainty metrics at even 66% confidence (0.06 ± 0.13 and 0.06 ± 0.09 W m^{-2} decade^{-1}, respectively). This implies that the net cloud feedback is about as likely as not positive or negative (Mastrandrea et al. 2010), i.e., it could amplify or diminish global warming.

These cloud feedback trend results are consistent with Table 3's cloud feedbacks in traditional units of W m^{-2} K^{-1}. Our nonsignificant net cloud feedback of 0.20 ± 0.34 W m^{-2} K^{-1} stands in contrast to previous studies that found the observed net cloud feedback to be 0.4–0.7 W m^{-2} K^{-1} (Ceppi and Nowack 2021; Chao and Dessler 2021; Chao et al. 2022; Dessler 2010, 2013; Dessler and Loeb 2013). This discrepancy arises from most studies having an observed LW cloud feedback that is positive (0.1–0.6 W m^{-2} K^{-1}), in contrast to our significant negative LW cloud feedback of -0.38 ± 0.18 W m^{-2} K^{-1}, and the studies had an observed positive SW cloud feedback (0–0.3 W m^{-2} K^{-1}) that is smaller in magnitude than our estimate of 0.58 ± 0.44 W m^{-2} K^{-1} (Ceppi and Nowack 2021; Dessler 2010, 2013; Dessler and Loeb 2013; Yue et al. 2019; Zhou et al. 2013).

Climate models in short-term and long-term simulations also display large net cloud feedbacks (0.3–0.8 W m^{-2} K^{-1}) that arise from additive positive LW (0.3–0.6 W m^{-2} K^{-1}) and SW (0–0.3 W m^{-2} K^{-1}) cloud feedbacks, with LW being the dominant factor (Ceppi and Nowack 2021; Chao and Dessler 2021; Chao et al. 2022; Dessler 2010, 2013; Soden and Held 2006; Zelinka et al. 2020; Zhou et al. 2015). Models from this study also overestimate the cloud feedback. By subtracting ERA5-PRP's cloud-masking estimate from the multimodel-mean ΔW_{CRE}, we obtain a 0.23 W m^{-2} decade^{-1} for the net cloud feedback, a large overestimation of the observed net cloud feedback trend. Even in AMIP conditions, GFDL AM4 shows biases in the cloud feedback trend. By subtracting AM4's cloud-masking estimate (Table 2) from ΔW_{CRE} (AM4 PSST), we obtain a 0.09 W m^{-2} decade^{-1} for the net cloud feedback. However, we find that the relatively lower

TABLE 3. Global-mean cloud feedback and CRE "feedback" estimates derived from CERES radiation observations and GISTEMP surface temperature anomalies during January 2001–December 2020 [appendix, Eq. (A4b)]. λ_{cloud} is calculated using AM4 ERF for the estimate of ERF. λ_{CRE} is calculated by regressing monthly mean anomalies in observed CRE against GISTEMP surface temperature; i.e., it includes all factors including ERF and cloud masking [Eqs. (1) and (A4b)]. This was done to show that if cloud feedback was calculated like λ_{CRE}, an inflated value would be obtained for LW and SW. Uncertainty is given by the 95% CI that is derived from 2σ spread of λ_{CRE} values, i.e., $\varepsilon_{\lambda_{CRE}}$, in GFDL AM4 PSST (20 AMIP realizations). Units are W m^{-2} K^{-1}.

Quantity	Cloud feedback (λ_{cloud})	CRE feedback (λ_{CRE})
LW CERES	-0.38 ± 0.18	-0.72 ± 0.18
SW CERES	0.58 ± 0.44	0.83 ± 0.44
Net CERES	0.20 ± 0.34	0.11 ± 0.34

overestimation is because of compensating errors in LW and SW: a weakly positive LW cloud feedback and a near-zero SW cloud feedback rather than the observed cancelling negative and positive LW and SW cloud feedbacks, respectively.

5. Discussion

Recent studies have decomposed CRE changes into cloud-controlling factors (Andersen et al. 2022; Klein et al. 2017; Scott et al. 2020). Our study suggests that such an analysis should include forcing in the cloud controlling factors or remove forcing from their SST-mediated controlling factors. Our study showed that using CRE as a proxy for cloud feedback is a poor approximation since CRE is a combination of various factors (Fig. 6, Table 3, appendix).

Another example of showing how ΔCRE cannot be used directly for determining cloud feedback, because it is a convolution of forcing, cloud masking, and cloud feedbacks, can be seen in CERES-FBCT outputs of vertical and optical depth resolved trends in CRE (Fig. 7). For example, it is known that clouds close to the surface have a temperature close to the surface's, so they are ineffective in preventing the escape of infrared radiation to space, i.e., low clouds have little impact on LWCRE while high clouds have a large impact on LWCRE (e.g., Zelinka and Hartmann 2010). Yet, Fig. 7a shows significant negative LWCRE trends coming from the lower troposphere. Given our cloud-masking results (Fig. 5), we can infer that the LWCRE trend here is likely not due to low cloud changes but due to water vapor and well-mixed greenhouse gas cloud masking. Similarly, SWCRE shows significant positive trends in the lower troposphere which stem from cloud cover and liquid water path (LWP) decreases (Figs. 7b,d). However, the cloud cover changes and the LWP changes are not just SST-mediated but are likely influenced by greenhouse gas adjustments and the aerosol-indirect effect (Figs. 2b and 3b, supplemental Fig. 5). Thus, we recommend future studies take caution when interpreting FBCT and FBCT-like observational fluxes and to remove forcing and masking before inferring feedbacks in the observational record.

Our observationally derived net cloud feedback is small because of large LW and SW cloud feedbacks of opposite signs while previous observational studies have a large net cloud feedback because of additive positive LW and SW cloud feedbacks (Ceppi and Nowack 2021; Dessler 2010, 2013; Dessler and Loeb 2013; Yue et al. 2019). Two exceptions to this generalization are the observational studies of Chao and Dessler (2021) and Zhou et al. (2013). A negative LW cloud feedback in observations is also supported by Loeb et al. (2021b) and de Guélis et al. (2018) although these studies do not separate forcing from feedback and CRE from cloud feedback, respectively. The observed significant negative LW cloud feedback in our study as well as evidence supporting this finding from the above studies demands more attention and investigation in future studies. It is important to decipher the mechanisms that cause the negative LW cloud feedback because 1) it is unclear why some observational studies disagree not only in magnitude but also in the sign of the LW cloud feedback, 2) it is unclear why models in short-term and long-term simulations are missing a negative LW cloud feedback, and 3) it is an unexpected result in light of the well-established positive altitude LW cloud feedback (e.g., Zelinka and Hartmann 2010). One possible mechanism for this negative LW cloud feedback is a negative tropical anvil cloud area feedback as suggested by Sherwood et al. (2020). Figure 7f suggests decreases in ice water path (IWP) as another pathway that could explain this negative LW cloud feedback.

We note that the potentially larger ΔERF_{SWCRE} trend from a larger aerosol decline in the updated CEDS would reduce the observationally derived positive SW cloud feedback's magnitude and hence make the net cloud feedback's magnitude even closer to 0 or even slightly negative. Changing patterns of SST warming can also cause a divergence between observed feedbacks and simulated historical and future feedbacks in coupled model simulations (Andrews et al. 2022; Dong et al. 2021). Additionally, although we find consistency between the cloud feedbacks estimated from monthly-mean anomalies (Table 3) and cloud feedback decadal trends (Fig. 6), the latter method's results are less susceptible to changing the start and end dates of the time period (supplemental Fig. 4).

Finally, it is worth noting that the observational uncertainty that sets detectability has uncertainty itself. The R21 observational uncertainty would preclude measuring a detectable cloud feedback at 95% confidence even by 2050 (supplemental Fig. 3). Assessing whether the "true" observational uncertainty is more like R21 or L21 should be a priority for future observational studies, since this will not only enhance confidence in existing observational trends but also provide better constraints for climate models.

6. Summary and conclusions

We showed that the observed global-mean trends in LWCRE and SWCRE are extremely unlikely to be due to unforced variability alone (Fig. 1). SWCRE ERF was found to have a large enough signal that it could account for slightly over half of the observed positive SWCRE trend via cloud adjustments (greenhouse gas increases, aerosol decreases, and natural forcing agents) (Figs. 2 and 3). The role of ERF was highlighted regionally, and it was shown that the PDO has little impact on the flux changes in the northeast Pacific (Fig. 3). We found that cloud masking, arising from ERF and surface warming, yielded a strongly negative trend in LWCRE since greenhouse gases reduce OLR in clear-sky conditions more than in all-sky conditions and could account for slightly over half of the observed negative LWCRE trend (Figs. 4 and 5 and Table 2). Supplementing the large ERF and cloud-masking contributions to the LW and SW CRE trends were the LW and SW cloud feedback trends that accounted for just under half of the observed LW and SW CRE trends (Fig. 6). The negative LW cloud feedback and positive SW cloud feedback trends were detectable at 80%–95% confidence depending on the observational uncertainty assumed. As a result of the strongly cancelling LW and SW cloud feedbacks, the net cloud feedback was found to be unconstrained in sign over the modern satellite

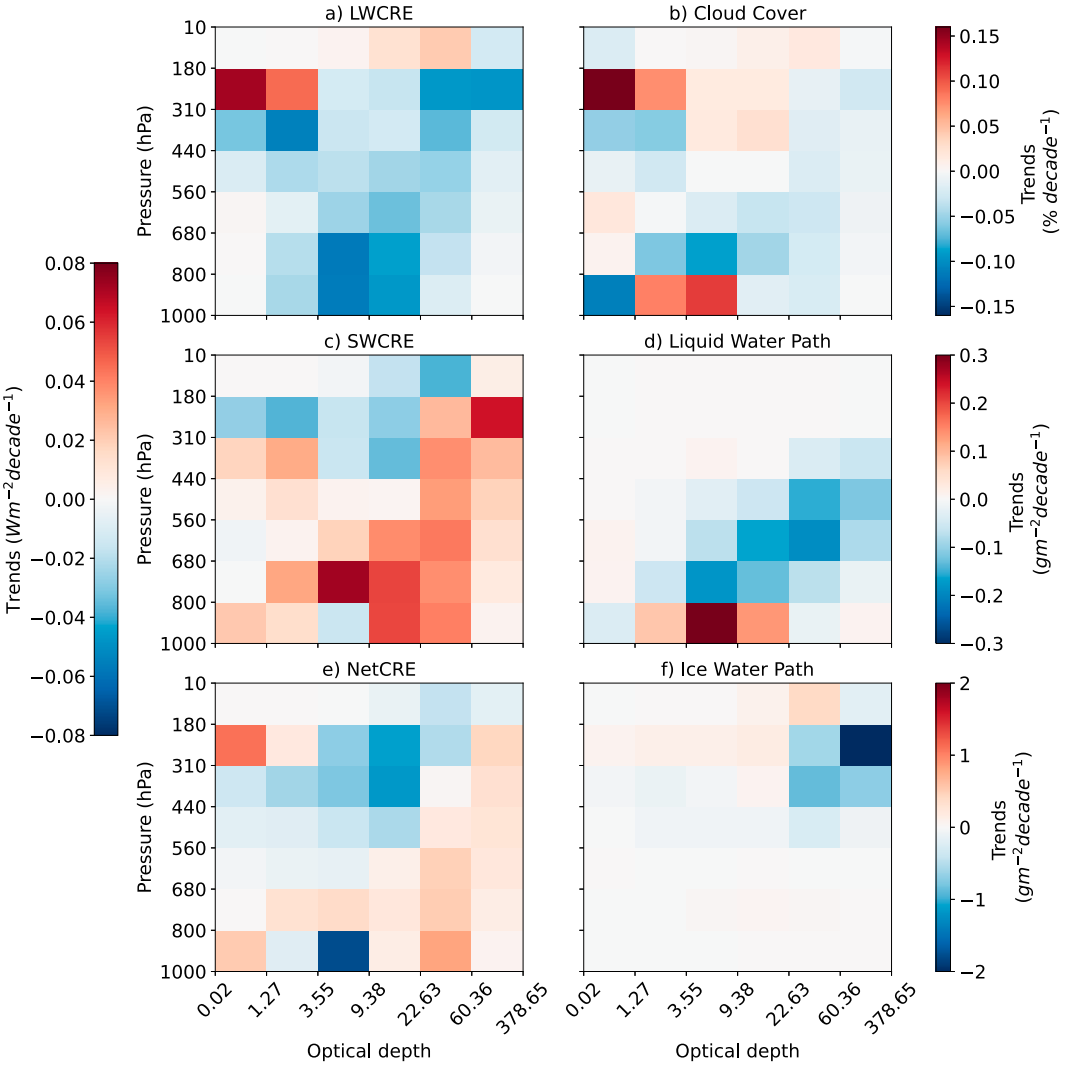

FIG. 7. CERES-FBCT trends during July 2002–July 2020 for the near-global average (58°S–58°N). (a),(c),(e) LW, SW, Net CRE trends, respectively. CREs are calculated for each grid point and bin using Eq. (5) of Scott et al. (2020), then area-averaged, and then the trends are computed. (b),(d),(f) Cloud cover, liquid water path (LWP), and ice water path (IWP) trends. LWP and IWP are cloud-fraction weighted.

era (Fig. 6). Finally, we cautioned the interpretation of CRE as cloud feedback (Table 3 and Fig. 7).

More broadly, this study helps provide a deeper understanding of how heat is accumulating on the planet. This understanding is allowed by the excellent consistency in radiation budget changes between datasets: EEI increases were found with independent measurements (Allison et al. 2020; Hakuba et al. 2021; Kramer et al. 2021; Loeb et al. 2021b; Raghuraman et al. 2021a), we have found excellent consistency between CERES and the Atmospheric Infrared Sounder (AIRS) satellite all-sky LW fluxes (Raghuraman 2021), and there is good consistency between independent Earthshine measurements of RSW and CERES (Goode et al. 2021). The classical picture of an increased greenhouse effect from increases in greenhouse gases is correct, however, it gets cancelled by increased surface and atmospheric emission (GFDL AM4 clear-sky LW ERF ~0.35 W m^{-2} $decade^{-1}$ and clear-sky LW $\lambda\Delta T_s \sim -0.38$ W m^{-2} $decade^{-1}$; Raghuraman et al. 2019, 2021a). This study then showed that the mere presence of clouds in a warming climate and with increasing greenhouse gas concentrations, increases LW emission relative to clear skies (−0.19 W m^{-2} $decade^{-1}$; Fig. 5a's LWCRE total cloud masking). This implies that we do not need to invoke high cloud cover reductions (Norris 2005; Trenberth and Fasullo 2009) to explain the majority of the observed LWCRE decrease. In fact, Fig. 7b instead shows increases in high cloud cover since 2002 (not significant). The LW cloud feedback explains the rest of the LWCRE decrease but its causes need further investigation (see section 5) (−0.15 W m^{-2} $decade^{-1}$).

The observed increase in Earth's energy imbalance therefore does not come from LW changes (CERES all-sky LW ~−0.28 W m^{-2} $decade^{-1}$) but instead from decreased SW

reflection (~0.70 W m^{-2} $decade^{-1}$) (Raghuraman et al. 2021a). Previously it was surmised that the decreased reflection would manifest through the SW water vapor feedback and the ice–albedo feedback (Donohoe et al. 2014), however, we find that these are minority contributors (water vapor ~0.07 W m^{-2} $decade^{-1}$ and surface albedo ~0.15 W m^{-2} $decade^{-1}$; supplemental Tables 1 and 2). Instead, we find that the majority of the decreased reflection arises from SW ERF increases (~0.28 W m^{-2} $decade^{-1}$; Raghuraman et al. 2021a) and the SW cloud feedback (~0.21 W m^{-2} $decade^{-1}$). Put simply, in response to external forcing in LW and SW radiation, Earth has a stabilizing feedback only in the LW and not in the SW, so the planet accumulates heat in the SW.

Acknowledgments. We thank the three anonymous reviewers for their constructive feedback. We thank Leo Donner and Yi Ming for internally reviewing this manuscript. Numerical simulations were conducted with GFDL computational resources. S.P.R. was supported by the Future Investigators in NASA Earth and Space Science and Technology Award 80NSSC19K1372 and partially supported by the High Meadows Environmental Institute at Princeton University through the Mary and Randall Hack '69 Research Fund. We acknowledge the World Climate Research Programme, which, through its Working Group on Coupled Modelling, coordinated and promoted CMIP6. We thank the climate modeling groups for producing and making available their model output, the Earth System Grid Federation (ESGF) for archiving the data and providing access, and the multiple funding agencies that support CMIP6 and ESGF.

Data availability statement. CERES EBAF Edition 4.1 observational data were retrieved from the NASA Langley Research Center Atmospheric Science Data Center (https://ceres.larc.nasa.gov/data/). The observed surface temperature was obtained from GISTEMP Team (2023). CMIP6 Control, Historical, and RFMIP data were obtained from the CMIP6 archive (https://esgf-node.llnl.gov/projects/cmip6/). The GFDL AM4 AMIP and Control data used in this study are in the Zenodo database under accession code https://doi.org/10.5281/zenodo.4784726 (Raghuraman et al. 2021b). ERA5-PRP data generated in this study have been deposited in the Zenodo database under accession code https://doi.org/10.5281/zenodo.7623726 (Raghuraman et al. 2023). Code can be accessed at https://doi.org/10.5281/zenodo.7623105 (Raghuraman 2023).

APPENDIX

Partial Radiation Perturbation Experiment Methodology

Let R be the radiation emanating at the top-of-atmosphere, i.e., outgoing longwave radiation (OLR) or reflected shortwave radiation (RSW). A monthly anomaly in R can be decomposed into

$$\Delta R^{\text{clear}} = \Delta R^{\text{clear}}_{\text{WMGHG}} + \Delta R^{\text{clear}}_{O_3} + \Delta R^{\text{clear}}_{H_2O} + \Delta R^{\text{clear}}_{T_a} + \Delta R^{\text{clear}}_{T_s} + \Delta R^{\text{clear}}_{\alpha}, \tag{A1a}$$

$$\Delta R^{\text{all}} = \Delta R^{\text{all}}_{\text{WMGHG}} + \Delta R^{\text{all}}_{O_3} + \Delta R^{\text{all}}_{H_2O} + \Delta R^{\text{all}}_{T_a} + \Delta R^{\text{all}}_{T_s} + \Delta R^{\text{all}}_{\alpha} + \Delta R^{\text{all}}_{\text{cloud}}. \tag{A1b}$$

Here, WMGHG represents well-mixed greenhouse gases (CO_2, CH_4, N_2O, CFCs, HFCs), O_3 represents ozone, H_2O represents water vapor specific humidity, T_a represents atmospheric temperature, T_s represents surface temperature, α represents surface albedo, and "cloud" represents cloud properties (cloud cover, liquid water content, and ice water content).

The impact of changes in a particular quantity, say surface temperature, on all-sky TOA radiation is calculated by the two-sided PRP (Colman and McAvaney 1997):

$$\begin{aligned}\Delta R^{\text{all}}_{T_s} = \frac{1}{2}[&R(\text{WMGHG}, O_3, H_2O, T_a, T_s, \alpha, \text{cloud}) \\ &- R(\text{WMGHG}, O_3, H_2O, T_a, \overline{T}_s, \alpha, \text{cloud})] \\ &+ \frac{1}{2}[R(\overline{\text{WMGHG}}, \overline{O_3}, \overline{H_2O}, \overline{T_a}, T_s, \overline{\alpha}, \overline{\text{cloud}}) \\ &- R(\overline{\text{WMGHG}}, \overline{O_3}, \overline{H_2O}, \overline{T_a}, \overline{T}_s, \overline{\alpha}, \overline{\text{cloud}})].\end{aligned} \tag{A2}$$

The overbars indicate the monthly climatology for the time period. Overall, it captures the flux change solely due to a surface temperature change under two base states, one with all quantities at their varied state and one with all quantities at their climatology state. Both states, i.e., both sides of the PRP, are then averaged out to give a symmetric and best estimate. This two-sided PRP is similarly applied to all other variables, and we conduct eight experiments in total: one for each variable listed above and one for the total [first term and last term of the four terms on the right-hand side of Eq. (A2)].

In the context of CRE, which is the difference between clear-sky and all-sky flux, we can write an anomaly in CRE as

$$\begin{aligned}\Delta\text{CRE} = &(\Delta R^{\text{clear}}_{\text{WMGHG}} - \Delta R^{\text{all}}_{\text{WMGHG}}) + (\Delta R^{\text{clear}}_{O_3} - \Delta R^{\text{all}}_{O_3}) \\ &+ (\Delta R^{\text{clear}}_{H_2O} - \Delta R^{\text{all}}_{H_2O}) + (\Delta R^{\text{clear}}_{T_a} - \Delta R^{\text{all}}_{T_a}) \\ &+ (\Delta R^{\text{clear}}_{T_s} - \Delta R^{\text{all}}_{T_s}) + (\Delta R^{\text{clear}}_{\alpha} - \Delta R^{\text{all}}_{\alpha}) \\ &+ (0 - \Delta R^{\text{all}}_{\text{cloud}}),\end{aligned} \tag{A3a}$$

$$\begin{aligned}\Delta\text{CRE} = &(\Delta\text{CRE}_{\text{WMGHG}} + \Delta\text{CRE}_{O_3} + \Delta\text{CRE}_{H_2O} \\ &+ \Delta\text{CRE}_{T_a} + \Delta\text{CRE}_{T_s} + \Delta\text{CRE}_{\alpha}) \\ &+ \Delta\text{CRE}_{\text{cloud}},\end{aligned} \tag{A3b}$$

$$\Delta\text{CRE} = \Delta\text{CRE}_{\text{cloud-masking}} + \Delta\text{CRE}_{\text{cloud}}. \tag{A3c}$$

This equation shows that the cloud radiative effect is the sum of the cloud and cloud-masking components. By combining Eqs. (1) and (A3c), we obtain:

$$\Delta\mathrm{CRE} = (\Delta\mathrm{ERF}_{\text{cloud-masking}} + \Delta\mathrm{ERF}_{\text{cloud}}) + (\Delta W_{\text{cloud-masking}} + \Delta W_{\text{cloud}}) + (\epsilon_{\text{cloud-masking}} + \epsilon_{\text{cloud}}), \quad \text{(A4a)}$$

$$\Delta\mathrm{CRE} = \Delta\mathrm{ERF}_{\mathrm{CRE}} + (\Delta W_{\text{cloud-masking}} + \Delta W_{\text{cloud}}) + \epsilon_{\mathrm{CRE}}. \quad \text{(A4b)}$$

Note that in Eqs. (1) and (A4b), ϵ_{CRE} is a particular value that satisfies this equation but in a 20-yr period there is a range of internal variability values that could satisfy this equation so ϵ_{CRE} is reported as a range in the paper. To compute ΔW_{cloud}, the cloud feedback trend, we obtain an observationally derived estimate by subtracting the forcing and cloud masking from the observed total CRE. Throughout this study, trends are calculated via linear fits through monthly anomalies time series, although calculating via annual-mean anomalies results in the same value of the trend.

REFERENCES

Allison, L. C., M. D. Palmer, R. P. Allan, L. Hermanson, C. Liu and D. M. Smith, 2020: Observations of planetary heating since the 1980s from multiple independent datasets. *Environ. Res. Commun.*, **2**, 101001, https://doi.org/10.1088/2515-7620/abbb39.

Andersen, H., J. Cermak, L. Zipfel, T. A. Myers, 2022: Attribution of observed recent decrease in low clouds over the northeastern Pacific to cloud-controlling factors. *Geophys. Res. Lett.*, **49**, e2021GL096498, https://doi.org/10.1029/2021GL096498.

Andrews, T., C. J. Smith, G. Myhre, P. M. Forster, R. Chadwick, and D. Ackerley, 2021: Effective radiative forcing in a GCM with fixed surface temperatures. *J. Geophys. Res. Atmos.*, **126**, e2020JD033880, https://doi.org/10.1029/2020JD033880.

——, and Coauthors, 2022: On the effect of historical SST patterns on radiative feedback. *J. Geophys. Res. Atmos.*, **127**, e2022JD036675, https://doi.org/10.1029/2022JD036675.

Bellomo, K., A. C. Clement, J. R. Norris, and B. J. Soden, 2014: Observational and model estimates of cloud amount feedback over the Indian and Pacific Oceans. *J. Climate*, **27**, 925–940, https://doi.org/10.1175/JCLI-D-13-00165.1.

Block, K., and T. Mauritsen, 2013: Forcing and feedback in the MPI-ESM-LR coupled model under abruptly quadrupled CO_2. *J. Adv. Model. Earth Syst.*, **5**, 676–691, https://doi.org/10.1002/jame.20041.

Brient, F., and T. Schneider, 2016: Constraints on climate sensitivity from space-based measurements of low-cloud reflection. *J. Climate*, **29**, 5821–5835, https://doi.org/10.1175/JCLI-D-15-0897.1.

Ceppi, P., and P. Nowack, 2021: Observational evidence that cloud feedback amplifies global warming. *Proc. Natl. Acad. Sci. USA*, **118**, e2026290118, https://doi.org/10.1073/pnas.2026290118.

Cesana, G., A. D. Del Genio, A. S. Ackerman, M. Kelley, G. Elsaesser, A. M. Fridlind, Y. Cheng, and M.-S. Yao, 2019: Evaluating models' response of tropical low clouds to SST forcings using CALIPSO observations. *Atmos. Chem. Phys.*, **19**, 2813–2832, https://doi.org/10.5194/acp-19-2813-2019.

Cesana, G. V., and A. D. Del Genio, 2021: Observational constraint on cloud feedbacks suggests moderate climate sensitivity. *Nat. Climate Change*, **11**, 213–218, https://doi.org/10.1038/s41558-020-00970-y.

Chao, L.-W., and A. E. Dessler, 2021: An assessment of climate feedbacks in observations and climate models using different energy balance frameworks. *J. Climate*, **34**, 9763–9773, https://doi.org/10.1175/JCLI-D-21-0226.1.

Chao, L.-W., J. C. Muller, and A. E. Dessler, 2022: Impacts of the unforced pattern effect on the cloud feedback in CERES observations and climate models. *Geophys. Res. Lett.*, **49**, e2021GL096299, https://doi.org/10.1029/2021GL096299.

Clark, J. P., E. E. Clothiaux, S. B. Feldstein, S. Lee, 2021: Drivers of global clear sky surface downwelling longwave irradiance trends from 1984 to 2017. *Geophys. Res. Lett.*, **48**, e2021GL093961, https://doi.org/10.1029/2021GL093961.

Clement, A. C., R. Burgman, and J. R. Norris, 2009: Observational and model evidence for positive low-level cloud feedback. *Science*, **325**, 460–464, https://doi.org/10.1126/science.1171255.

Colman, R. A., and B. J. McAvaney, 1997: A study of general circulation model climate feedbacks determined from perturbed sea surface temperature experiments. *J. Geophys. Res.*, **102**, 19 383–19 402, https://doi.org/10.1029/97JD00206.

de Guélis, V. T., H. Chepfer, R. Guzman, M. Bonazzola, D. M. Winker, V. Noel, 2018: Space lidar observations constrain longwave cloud feedback. *Sci. Rep.*, **8**, 16570, https://doi.org/10.1038/s41598-018-34943-1.

Dessler, A. E., 2010: A determination of the cloud feedback from climate variations over the past decade. *Science*, **330**, 1523–1527, https://doi.org/10.1126/science.1192546.

——, 2013: Observations of climate feedbacks over 2000–10 and comparisons to climate models. *J. Climate*, **26**, 333–342, https://doi.org/10.1175/JCLI-D-11-00640.1.

——, and N. G. Loeb, 2013: Impact of dataset choice on calculations of the short-term cloud feedback. *J. Geophys. Res. Atmos.*, **118**, 2821–2826, https://doi.org/10.1002/jgrd.50199.

Dong, Y., and Coauthors, 2021: Biased estimates of equilibrium climate sensitivity and transient climate response derived from historical CMIP6 simulations. *Geophys. Res. Lett.*, **48**, e2021GL095778, https://doi.org/10.1029/2021GL095778.

Donohoe, A., K. C. Armour, A. G. Pendergrass, and D. S. Battisti, 2014: Shortwave and longwave radiative contributions to global warming under increasing CO_2. *Proc. Natl. Acad. Sci. USA*, **111**, 16 700–16 705, https://doi.org/10.1073/pnas.1412190111.

Eyring, V., S. Bony, G. A. Meehl, C. A. Senior, B. Stevens, R. J. Stouffer, and K. E. Taylor, 2016: Overview of the Coupled Model Intercomparison Project phase 6 (CMIP6) experimental design and organization. *Geosci. Model Dev.*, **9**, 1937–1958, https://doi.org/10.5194/gmd-9-1937-2016.

Forster, P., and Coauthors, 2021: The Earth's energy budget, climate feedbacks, and climate sensitivity. *Climate Change 2021: The Physical Science Basis*, V. Masson-Delmotte et al., Eds., Cambridge University Press, 923–1054.

Gelaro, R., and Coauthors, 2017: The Modern-Era Retrospective Analysis for Research and Applications, version 2 (MERRA-2). *J. Climate*, **30**, 5419–5454, https://doi.org/10.1175/JCLI-D-16-0758.1.

Gidden, M. J., and Coauthors, 2019: Global emissions pathways under different socioeconomic scenarios for use in CMIP6: A dataset of harmonized emissions trajectories through the end of the century. *Geosci. Model Dev.*, **12**, 1443–1475, https://doi.org/10.5194/gmd-12-1443-2019.

GISTEMP Team, 2023: GISS Surface Temperature Analysis (GISTEMP), version 4. NASA Goddard Institute for Space Studies, accessed 29 March 2021, https://data.giss.nasa.gov/gistemp/.

Goode, P. R., E. Pallé, A. Shoumko, S. Shoumko, P. Montañes-Rodriguez, and S. E. Koonin, 2021: Earth's albedo 1998–2017

as measured from earthshine. *Geophys. Res. Lett.*, **48**, e2021GL094888, https://doi.org/10.1029/2021GL094888.

Gregory, J., and M. Webb, 2008: Tropospheric adjustment induces a cloud component in CO_2 forcing. *J. Climate*, **21**, 58–71, https://doi.org/10.1175/2007JCLI1834.1.

Hakuba, M. Z., T. Frederikse, and F. W. Landerer, 2021: Earth's energy imbalance from the ocean perspective (2005–2019). *Geophys. Res. Lett.*, **48**, e2021GL093624, https://doi.org/10.1029/2021GL093624.

Hersbach, H., and Coauthors, 2020: The ERA5 global reanalysis. *Quart. J. Roy. Meteor. Soc.*, **146**, 1999–2049, https://doi.org/10.1002/qj.3803.

Hoesly, R. M., and Coauthors, 2018: Historical (1750–2014) anthropogenic emissions of reactive gases and aerosols from the community emissions data system (CEDS). *Geosci. Model Dev.*, **11**, 369–408, https://doi.org/10.5194/gmd-11-369-2018.

Hofmann, D. J., J. H. Butler, E. J. Dlugokencky, J. W. Elkins, K. Masarie, S. A. Montzka, and P. Tans, 2006: The role of carbon dioxide in climate forcing from 1979 to 2004: Introduction of the annual greenhouse gas index. *Tellus*, **58B**, 614–619, https://doi.org/10.1111/j.1600-0889.2006.00201.x.

Klein, S. A., A. Hall, J. R. Norris, and R. Pincus, 2017: Low-cloud feedbacks from cloud-controlling factors: A review. *Shallow Clouds, Water Vapor, Circulation, and Climate Sensitivity*, Springer, 135–157.

Kramer, R. J., H. He, B. J. Soden, L. Oreopoulos, G. Myhre, P. M. Forster, and C. J. Smith, 2021: Observational evidence of increasing global radiative forcing. *Geophys. Res. Lett.*, **48**, e2020GL091585, https://doi.org/10.1029/2020GL091585.

Lenssen, N. J. L., G. A. Schmidt, J. E. Hansen, M. J. Menne, A. Persin, R. Ruedy, D. Zyss, 2019: Improvements in the GISTEMP uncertainty model. *J. Geophys. Res. Atmos.*, **124**, 6307–6326, https://doi.org/10.1029/2018JD029522.

Loeb, N. G., and D. R. Doelling, 2020: CERES energy balanced and filled (EBAF) from afternoon-only satellite orbits. *Remote Sens.*, **12**, 1280, https://doi.org/10.3390/rs12081280.

——, N. Manalo-Smith, W. Su, M. Shankar, and S. Thomas, 2016: CERES top-of-atmosphere Earth radiation budget climate data record: Accounting for in-orbit changes in instrument calibration. *Remote Sens.*, **8**, 182, https://doi.org/10.3390/rs8030182.

——, T. J. Thorsen, J. R. Norris, H. Wang, and W. Su, 2018a: Changes in Earth's energy budget during and after the "pause" in global warming: An observational perspective. *Climate*, **6**, 62, https://doi.org/10.3390/cli6030062.

——, and Coauthors, 2018b: Clouds and the Earth's Radiant Energy System (CERES) Energy Balanced and Filled (EBAF) top-of-atmosphere (TOA) edition-4.0 data product. *J. Climate*, **31**, 895–918, https://doi.org/10.1175/JCLI-D-17-0208.1.

——, and Coauthors, 2020a: Toward a consistent definition between satellite and model clear-sky radiative fluxes. *J. Climate*, **33**, 61–75, https://doi.org/10.1175/JCLI-D-19-0381.1.

——, and Coauthors, 2020b: New generation of climate models track recent unprecedented changes in Earth's radiation budget observed by CERES. *Geophys. Res. Lett.*, **47**, e2019GL086705, https://doi.org/10.1029/2019GL086705.

——, W. Su, N. Bellouin, and Y. Ming, 2021a: Changes in clear-sky shortwave aerosol direct radiative effects since 2002. *J. Geophys. Res. Atmos.*, **126**, e2020JD034090, https://doi.org/10.1029/2020JD034090.

——, G. C. Johnson, T. J. Thorsen, J. M. Lyman, F. G. Rose, and S. Kato, 2021b: Satellite and ocean data reveal marked increase in Earth's heating rate. *Geophys. Res. Lett.*, **48**, e2021GL093047, https://doi.org/10.1029/2021GL093047.

——, and Coauthors, 2022: Evaluating twenty-year trends in Earth's energy flows from observations and reanalyses. *J. Geophys. Res. Atmos.*, **127**, e2022JD036686, https://doi.org/10.1029/2022JD036686.

Lutsko, N. J., M. Popp, R. H. Nazarian, A. L. Albright, 2021: Emergent constraints on regional cloud feedbacks. *Geophys. Res. Lett.*, **48**, e2021GL092934, https://doi.org/10.1029/2021GL092934.

Mastrandrea, M. D., and Coauthors, 2010: Guidance note for lead authors of the IPCC fifth assessment report on consistent treatment of uncertainties. IPCC, 4 pp., https://www.ipcc.ch/site/assets/uploads/2018/05/uncertainty-guidance-note.pdf.

Myers, T. A., C. R. Mechoso, G. V. Cesana, M. J. DeFlorio, and D. E. Waliser, 2018: Cloud feedback key to marine heatwave off Baja California. *Geophys. Res. Lett.*, **45**, 4345–4352, https://doi.org/10.1029/2018GL078242.

——, R. C. Scott, M. D. Zelinka, S. A. Klein, J. R. Norris and P. M. Caldwell, 2021: Observational constraints on low cloud feedback reduce uncertainty of climate sensitivity. *Nat. Climate Change*, **11**, 501–507, https://doi.org/10.1038/s41558-021-01039-0.

Norris, J. R., 2005: Multidecadal changes in near-global cloud cover and estimated cloud cover radiative forcing. *J. Geophys. Res.*, **110**, D08206, https://doi.org/10.1029/2004JD005600.

O'Rourke, P. R, and Coauthors, 2021: CEDS v-2021-02-05 emission data 1975–2019 (version 5 February 2021). Zenodo, accessed 5 February 2021, https://zenodo.org/record/4509372#.ZAXA8nZByUk.

Pincus, R., R. Hemler, and S. A. Klein, 2006: Using stochastically generated subcolumns to represent cloud structure in a large-scale model. *Mon. Wea. Rev.*, **134**, 3644–3656, https://doi.org/10.1175/MWR3257.1.

——, P. M. Forster, and B. Stevens, 2016: The Radiative Forcing Model Intercomparison Project (RFMIP): Experimental protocol for CMIP6. *Geosci. Model Dev.*, **9**, 3447–3460, https://doi.org/10.5194/gmd-9-3447-2016.

——, E. J. Mlawer, and J. S. Delamere, 2019: Balancing accuracy, efficiency, and flexibility in radiation calculations for dynamical models. *J. Adv. Model. Earth Syst.*, **11**, 3074–3089, https://doi.org/10.1029/2019MS001621.

Raghuraman, S. P., 2021: Changes in the satellite-observed radiation budget: Manifestations of radiative forcing, feedbacks, and internal variability. Ph.D. dissertation, Princeton University, 179 pp.

——, 2023: Forcing, cloud feedbacks, cloud masking, and internal variability in the cloud radiative effect satellite record (code). Zenodo, https://doi.org/10.5281/zenodo.7623105.

——, D. Paynter, and V. Ramaswamy, 2019: Quantifying the drivers of the clear sky greenhouse effect, 2000–2016. *J. Geophys. Res. Atmos.*, **124**, 11 354–11 371, https://doi.org/10.1029/2019JD031017.

——, ——, and ——, 2021a: Anthropogenic forcing and response yield observed positive trend in Earth's energy imbalance. *Nat. Commun.*, **12**, 4577, https://doi.org/10.1038/s41467-021-24544-4.

——, ——, and ——, 2021b: Anthropogenic forcing and response yield observed positive trend in Earth's energy imbalance (data). Zenodo, https://doi.org/10.5281/zenodo.4784726.

——, ——, R. Menzel, and V. Ramaswamy, 2023: Forcing, cloud feedbacks, cloud masking, and internal variability in the cloud radiative effect satellite record (data). Zenodo, https://doi.org/10.5281/zenodo.7623726.

Ramanathan, V., R. D. Cess, E. F. Harrison, P. Minnis, B. R. Barkstrom, E. Ahmad, and D. Hartmann, 1989: Cloud-radiative forcing and climate: Results from the Earth Radiation Budget experiment. *Science*, **243**, 57–63, https://doi.org/10.1126/science.243.4887.57.

Ramaswamy, V., and Coauthors, 2019: Radiative forcing of climate: The historical evolution of the radiative forcing concept, the forcing agents and their quantification, and applications. *A Century of Progress in Atmospheric and Related Sciences: Celebrating the American Meteorological Society Centennial*, *Meteor. Monogr.*, Vol. 59, https://doi.org/10.1175/AMSMONOGRAPHS-D-19-0001.1.

Romps, D. M., 2020: Climate sensitivity and the direct effect of carbon dioxide in a limited-area cloud-resolving model. *J. Climate*, **33**, 3413–3429, https://doi.org/10.1175/JCLI-D-19-0682.1.

Salvi, P., P. Ceppi, and J. M. Gregory, 2021: Interpreting the dependence of cloud-radiative adjustment on forcing agent. *Geophys. Res. Lett.*, **48**, e2021GL093616, https://doi.org/10.1029/2021GL093616.

Schneider, T., C. M. Kaul, and K. G. Pressel, 2019: Possible climate transitions from breakup of stratocumulus decks under greenhouse warming. *Nature Geosci.*, **12**, 163–167, https://doi.org/10.1038/s41561-019-0310-1.

Scott, R. C., T. A. Myers, J. R. Norris, M. D. Zelinka, S. A. Klein, M. Sun, and D. R. Doelling, 2020: Observed sensitivity of low-cloud radiative effects to meteorological perturbations over the global oceans. *J. Climate*, **33**, 7717–7734, https://doi.org/10.1175/JCLI-D-19-1028.1.

Shankar, M., W. Su, N. Manalo-Smith, and N. G. Loeb, 2020: Generation of a seamless Earth radiation budget climate data record: A new methodology for placing overlapping satellite instruments on the same radiometric scale. *Remote Sens.*, **12**, 2787, https://doi.org/10.3390/rs12172787.

Sherwood, S. C., and Coauthors, 2020: An assessment of Earth's climate sensitivity using multiple lines of evidence. *Rev. Geophys.*, **58**, e2019RG000678, https://doi.org/10.1029/2019RG000678.

Soden, B. J., and I. M. Held, 2006: An assessment of climate feedbacks in coupled ocean–atmosphere models. *J. Climate*, **19**, 3354–3360, https://doi.org/10.1175/JCLI3799.1.

——, A. J. Broccoli, and R. S. Hemler, 2004: On the use of cloud forcing to estimate cloud feedback. *J. Climate*, **17**, 3661–3665, https://doi.org/10.1175/1520-0442(2004)017<3661:OTUOCF>2.0.CO;2.

——, I. M. Held, R. Colman, K. M. Shell, J. T. Kiehl, and C. A. Shields, 2008: Quantifying climate feedbacks using radiative kernels. *J. Climate*, **21**, 3504–3520, https://doi.org/10.1175/2007JCLI2110.1.

Sun, M., D. R. Doelling, N. G. Loeb, R. C. Scott, J. Wilkins, L. T. Nguyen, and P. Mlynczak, 2022: Clouds and the Earth's Radiant Energy System (CERES) FluxByCldTyp edition 4 data product. *J. Atmos. Oceanic Technol.*, **39**, 303–318, https://doi.org/10.1175/JTECH-D-21-0029.1.

Thorsen, T. J., S. Kato, N. G. Loeb, and F. G. Rose, 2018: Observation-based decomposition of radiative perturbations and radiative kernels. *J. Climate*, **31**, 10 039–10 058, https://doi.org/10.1175/JCLI-D-18-0045.1.

Tompkins, A. M., 2002: A prognostic parameterization for the subgrid-scale variability of water vapor and clouds in large-scale models and its use to diagnose cloud cover. *J. Atmos. Sci.*, **59**, 1917–1942, https://doi.org/10.1175/1520-0469(2002)059<1917:APPFTS>2.0.CO;2.

Trenberth, K. E., and J. T. Fasullo, 2009: Global warming due to increasing absorbed solar radiation. *Geophys. Res. Lett.*, **36**, L07706, https://doi.org/10.1029/2009GL037527.

Webb, M. J., and A. P. Lock, 2013: Coupling between subtropical cloud feedback and the local hydrological cycle in a climate model. *Climate Dyn.*, **41**, 1923–1939, https://doi.org/10.1007/s00382-012-1608-5.

——, and ——, 2020: Testing a physical hypothesis for the relationship between climate sensitivity and double-ITCZ bias in climate models. *J. Adv. Model. Earth Syst.*, **12**, e2019MS001999, https://doi.org/10.1029/2019MS001999.

——, and Coauthors, 2015a: The diurnal cycle of marine cloud feedback in climate models. *Climate Dyn.*, **44**, 1419–1436, https://doi.org/10.1007/s00382-014-2234-1.

——, and Coauthors, 2015b: The impact of parametrized convection on cloud feedback. *Philos. Trans. Roy. Soc.*, **373A**, 20140414, https://doi.org/10.1098/rsta.2014.0414.

——, A. P. Lock, and F. H. Lambert, 2018: Interactions between hydrological sensitivity, radiative cooling, stability, and low-level cloud amount feedback. *J. Climate*, **31**, 1833–1850, https://doi.org/10.1175/JCLI-D-16-0895.1.

Wilcox, E. M., G. Roberts, and V. Ramanathan, 2006: Influence of aerosols on the shortwave cloud radiative forcing from North Pacific oceanic clouds: Results from the Cloud Indirect Forcing Experiment (CIFEX). *Geophys. Res. Lett.*, **33**, L21804, https://doi.org/10.1029/2006GL027150.

Wu, H., X. Xu, T. Luo, Y. Yang, Z. Xiong, and Y. Wang, 2022: Variation and comparison of cloud cover in MODIS and four reanalysis datasets of ERA-interim, ERA5, MERRA-2 and NCEP. *Atmos. Res.*, **281**, 106477, https://doi.org/10.1016/j.atmosres.2022.106477.

Wyant, M. C., C. S. Bretherton, P. N. Blossey, and M. Khairoutdinov, 2012: Fast cloud adjustment to increasing CO_2 in a superparameterized climate model. *J. Adv. Model. Earth Syst.*, **4**, M05001, https://doi.org/10.1029/2011MS000092.

Yao, B., S. Teng, R. Lai, X. Xu, Y. Yin, C. Shi, and C. Liu, 2020: Can atmospheric reanalyses (CRA and ERA5) represent cloud spatiotemporal characteristics? *Atmos. Res.*, **244**, 105091, https://doi.org/10.1016/j.atmosres.2020.105091.

Yoshimori, M., F. H. Lambert, M. J. Webb, and T. Andrews, 2020: Fixed anvil temperature feedback: Positive, zero, or negative? *J. Climate*, **33**, 2719–2739, https://doi.org/10.1175/JCLI-D-19-0108.1.

Yue, Q., B. H. Kahn, E. J. Fetzer, S. Wong, X. Huang, and M. Schreier, 2019: Temporal and spatial characteristics of short-term cloud feedback on global and local interannual climate fluctuations from A-Train observations. *J. Climate*, **32**, 1875–1893, https://doi.org/10.1175/JCLI-D-18-0335.1.

Zelinka, M. D., and D. L. Hartmann, 2010: Why is longwave cloud feedback positive? *J. Geophys. Res.*, **115**, D16117, https://doi.org/10.1029/2010JD013817.

——, T. A. Myers, D. T. McCoy, S. Po-Chedley, P. M. Caldwell, P. Ceppi, S. A. Klein, and K. E. Taylor, 2020: Causes of higher climate sensitivity in CMIP6 models. *Geophys. Res. Lett.*, **47**, e2019GL085782, https://doi.org/10.1029/2019GL085782.

Zhao, M., and Coauthors, 2018: The GFDL global atmosphere and land model AM4. 0/LM4. 0: 1. Simulation characteristics with prescribed SSTs. *J. Adv. Model. Earth Syst.*, **10**, 691–734, https://doi.org/10.1002/2017MS001208.

Zhou, C., M. D. Zelinka, A. E. Dessler, and P. Yang, 2013: An analysis of the short-term cloud feedback using MODIS data. *J. Climate*, **26**, 4803–4815, https://doi.org/10.1175/JCLI-D-12-00547.1.

——, ——, ——, and S. A. Klein, 2015: The relationship between interannual and long-term cloud feedbacks. *Geophys. Res. Lett.*, **42**, 10 463–10 469, https://doi.org/10.1002/2015GL066698.